Longitudinal omics in Syrian hamsters integrated with human data unravel complexity of moderate immune responses to SARS-CoV-2

Geraldine Nouailles[1,2+*], Emanuel Wyler[3+*], Peter Pennitz[1], Dylan Postmus[2,4], Daria Vladimirova[5], Julia Kazmierski[2,4], Fabian Pott[2,4], Kristina Dietert[6,7], Michael Mülleder[8], Vadim Farztdinov[8], Benedikt Obermayer[9], Sandra-Maria Wienhold[1], Sandro Andreotti[10], Thomas Höfler[5], Birgit Sawitzki[11], Christian Drosten[4], Leif Erik Sander[12], Norbert Suttorp[12], Markus Ralser[13], Dieter Beule[9], Achim Dieter Gruber[6], Christine Goffinet[2,4], Markus Landthaler[14], Jakob Trimpert[5#*] and Martin Witzenrath[1,12,15#*]

+ shared first authorship with equal contributions

# shared senior authorship with equal contributions

* Corresponding authors:

Correspondence to Geraldine Nouailles (geraldine.nouailles@charite.de), Emanuel Wyler (emanuel.wyler@mdc-berlin.de), Jakob Trimpert (jakob.trimpert@fu-berlin.de), Martin Witzenrath (martin.witzenrath@charite.de)

[1] Division of Pulmonary Inflammation, Charité - Universitätsmedizin Berlin, corporate member of Freie Universität Berlin, Humboldt-Universität zu Berlin, and Berlin Institute of Health, Berlin, Germany.

[2] Berlin Institute of Health (BIH), Berlin, Germany.

[3] Berlin Institute for Medical Systems Biology (BIMSB), Max Delbrück Center for Molecular Medicine in the Helmholtz Association (MDC), Berlin, Germany.

[4] Institute of Virology, Charité - Universitätsmedizin Berlin, corporate member of Freie Universität Berlin, Humboldt-Universität zu Berlin and Berlin Institute of Health (BIH), Berlin, Germany.

[5] Institute of Virology, Freie Universität Berlin, Berlin, Germany.

[6] Institute of Veterinary Pathology, Freie Universität Berlin, Berlin, Germany.

[7] Veterinary Centre for Resistance Research, Freie Universität Berlin, Berlin, Germany.

[8] Core Facility - High-Throughput Mass Spectrometry, Charité - Universitätsmedizin Berlin, corporate member of Freie Universität Berlin, Humboldt-Universität zu Berlin and Berlin Institute of Health (BIH), Berlin, Germany.

[9] Core Unit Bioinformatics, Berlin Institute of Health (BIH), Max Delbrück Center for Molecular Medicine in the Helmholtz Association (MDC) and Charité - Universitätsmedizin, Berlin, Germany.
[10] Bioinformatics Solution Center, Freie Universität Berlin, Berlin, Germany.
[11] Institute of Medical Immunology. Charité - Universitätsmedizin Berlin, corporate member of Freie Universität Berlin, Humboldt-Universität zu Berlin, and Berlin Institute of Health, Berlin, Germany.
[12] Department of Infectious Diseases and Respiratory Medicine, Charité - Universitätsmedizin Berlin, corporate member of Freie Universität Berlin, Humboldt-Universität zu Berlin, and Berlin Institute of Health, Berlin, Germany.
[13] The Francis Crick Institute, Molecular Biology of Metabolism Laboratory, London, UK; Department of Biochemistry, Charité - Universitätsmedizin Berlin, corporate member of Freie Universität Berlin, Humboldt-Universität zu Berlin and Berlin Institute of Health (BIH), Berlin, Germany.
[14] Berlin Institute for Medical Systems Biology (BIMSB), Max Delbrück Center for Molecular Medicine in the Helmholtz Association (MDC), Berlin, Germany; IRI Life Sciences, Institute for Biology, Humboldt University Berlin, Berlin, Germany.
[15] German Center for Lung Research (DZL), Berlin, Germany.

Highlights

- Our hamster data allow for comparison and alignments with patient data
- Only few pulmonary epithelial cells are infected and show a weak response
- We provide kinetics and origin of SARS-CoV-2-induced mediator expression, including expression programs in endothelial cell subtypes
- Neutrophil recruitment is minor and resolved before peak inflammation
- Monocyte-derived macrophages and endothelial cell subtypes strongly activate pro-inflammatory and T cell attracting chemokine expression
- Cytotoxic effector $CD8^+$ and $CD4^+$ T cells are recruited and their arrival coincides with viral clearance and symptom cessation

In brief

Using omics tools with the SARS-CoV-2 infected Syrian hamster as model for COVID-19, along with published datasets from COVID-19 patients, Nouailles et al. present a detailed longitudinal analysis of systemic and pulmonary quantitative and qualitative

immune responses in a moderate disease setting. Targeted analysis of the alveolar and microvascular niche revealed a dominant role for monocyte-derived macrophages and endothelial cells regarding early anti-viral genes as well as pro-inflammatory and T cell recruiting chemokine expression. Recruitment of cytotoxic effector T cells coincided with viral clearance. This combined response was favorable for a moderate and self-limited disease course.

Graphical abstract

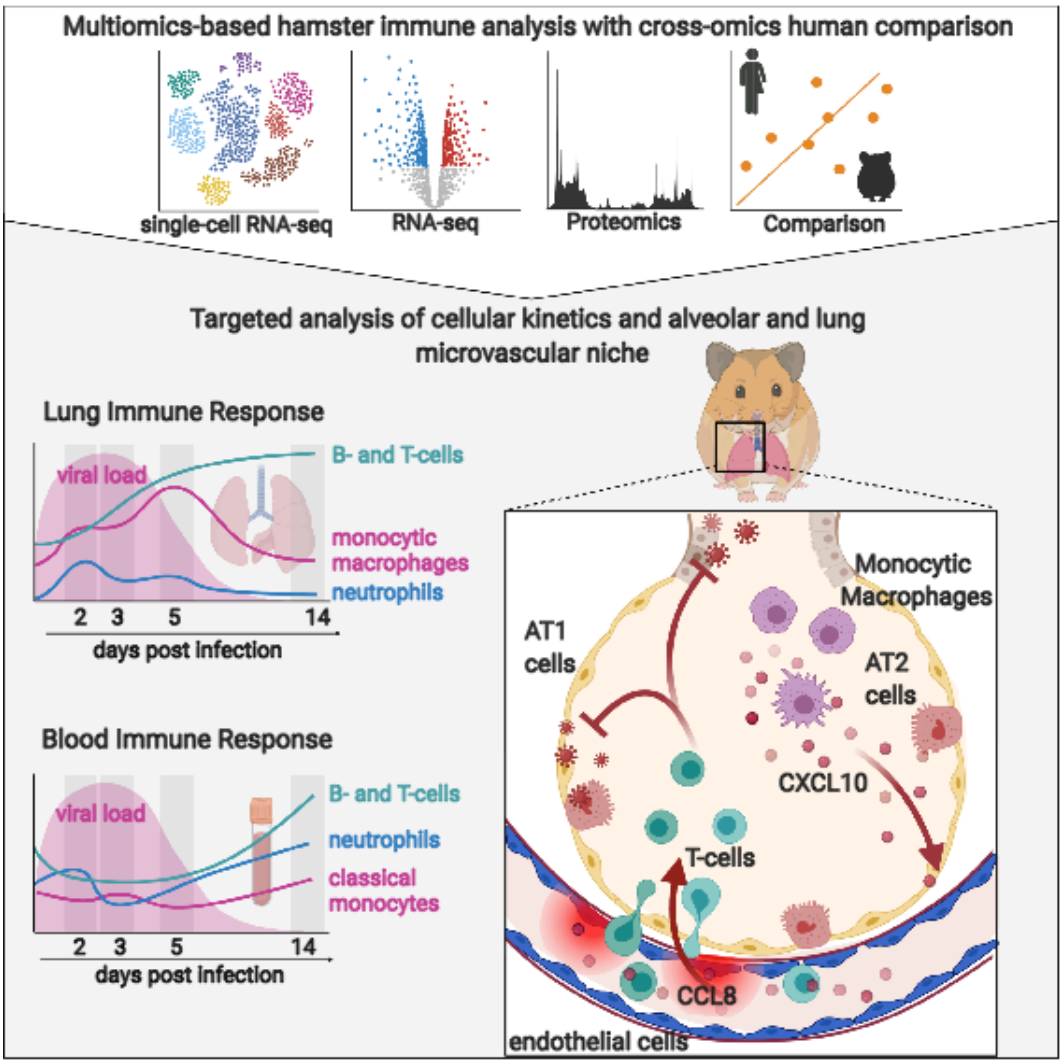

Summary

In COVID-19, the immune response largely determines disease severity and is key to therapeutic strategies. Cellular mechanisms contributing to inflammatory lung injury and tissue repair in SARS-CoV-2 infection, particularly endothelial cell involvement, remain ill-defined. We performed detailed spatiotemporal analyses of cellular and molecular processes in SARS-CoV-2 infected Syrian hamsters. Comparison of

hamster single-cell sequencing and proteomics with data sets from COVID-19 patients demonstrated inter-species concordance of cellular and molecular host-pathogen interactions. In depth vascular and pulmonary compartment analyses (i) supported the hypothesis that monocyte-derived macrophages dominate inflammation, (ii) revealed endothelial inflammation status and T-cell attraction, and (iii) showed that $CD4^+$ and $CD8^+$ cytotoxic T-cell responses precede viral elimination. Using the Syrian hamster model of self-limited moderate COVID-19, we defined the specific roles of endothelial and epithelial cells, among other myeloid and non-myeloid lung cell subtypes, for determining the disease course.

Keywords: coronavirus disease 2019; COVID-19; Syrian hamster; SARS-CoV-2; inflammatory monocytes; macrophages; cytotoxic T cells; endothelial cells

Introduction

The enduring severe acute respiratory syndrome coronavirus 2 (SARS-CoV-2) pandemic has emphasized the urgent need for experimental models to rapidly identify pathomechanisms and therapeutic targets of Corona Virus Disease 2019 (COVID-19). COVID-19 causes a wide range of disease manifestations, spanning from asymptomatic infections to acute respiratory distress syndrome (ARDS) and fatal multi-organ dysfunction (Guan et al., 2020). Disease severity is influenced by age, sex and specific comorbidities, making it evident that host-specific factors influence the course of the disease and require further investigation. While blood of COVID-19 patients is accessible to detailed longitudinal investigation, irrespective of disease severity, and bronchoalveolar lavage (BAL) can be safely performed in intubated patients, pulmonary tissue responses remain inaccessible in mild and moderate COVID-19 courses, since lung tissue is only available upon autopsy from patients with fatal disease. Hence, experimental models of COVID-19 are needed, which reflect the complexity of human responses to SARS-CoV-2 infections, including the spatiotemporal dynamics of airway and alveolar infection, local pulmonary immune responses, the activation of systemic inflammatory, complement and coagulation cascades, the impairment of endothelial barrier function, and also mechanisms of resilience, resolution and repair.

The hamster family (Cricetinae) is of particular interest for experimental modelling of COVID-19, as we and others have observed that animals without genetic modifications

117 can be infected with SARS-CoV-2 and develop phenotypes ranging from mild to lethal
118 COVID-19, depending on age and species (Bertzbach et al., 2020; Imai et al., 2020;
119 Osterrieder et al., 2020; Sia et al., 2020; Trimpert et al., 2020). Notably, immune cell
120 influx into the lungs, bronchointerstitial pneumonia and diffuse alveolar damage in
121 hamsters bear resemblance to COVID-19 in human patients (Gruber et al., 2020;
122 Kreye et al., 2020a; Lee et al., 2020).
123 Since its initial description as animal model for SARS-CoV (Roberts et al., 2005), the
124 Syrian hamster has been used to study different aspects of SARS-CoV and Middle
125 East Respiratory Syndrome (MERS) coronavirus infection (Gong and Bao, 2018;
126 Gretebeck and Subbarao, 2015; Subbarao and Roberts, 2006). Consequently, it now
127 serves as a versatile non-transgenic rodent model to study SARS-CoV-2 infection and
128 therapeutic interventions such as antiviral treatments, immunomodulatory therapies
129 and vaccines (Imai et al., 2020; Kreye et al., 2020b; Tostanoski et al., 2020). The
130 disease observed in hamster species primarily affects the lower respiratory tract, which
131 more closely resembles the common courses of human disease as opposed to
132 clinically severely affected transgenic mice, in many of which infection of the central
133 nervous system (CNS) is the predominant manifestation of the disease (Jiang et al.,
134 2020; Winkler et al., 2020).
135 Despite the advantages of hamster models for investigating COVID-19 pathogenesis,
136 unavailability of molecular tools and reagents for hamsters limits investigations of
137 immuno-pathomechanisms, leaving unanswered how closely SARS-CoV-2 evoked
138 disease in hamsters models human COVID-19. We therefore in-depth evaluated
139 SARS-CoV-2-infected Syrian hamsters (*Mesocricetus auratus*) elucidating the innate
140 and adaptive steps of immunity and pathogenesis by pairing single-cell RNA
141 sequencing (scRNA-Seq) data from lung cells and white blood cells (WBC),
142 histopathology and quantitative proteomics analysis of lungs and blood following nasal
143 SARS-CoV-2-infection of *Mesocricetus auratus*. We compared our findings with own
144 data from scRNA-Seq and proteomics analyses from human biosamples of COVID-19
145 patients. This enabled in-depth investigations on central COVID-19 pathomechanisms
146 in compartments inaccessible in humans, particularly in moderate disease.
147

Results

SARS-CoV-2 induces self-resolving moderate pneumonia and robust pulmonary immune cell recruitment in Syrian hamsters

After infection with SARS-CoV-2 (Figure S1), clinical disease manifested in Syrian hamsters with moderate transient weight loss analogous to previous reports ((Imai et al., 2020; Osterrieder et al., 2020; Sia et al., 2020), Figure S2a). High viral loads were detected in both the upper and lower respiratory tracts at 2, 3 and 5 days post infection (dpi). At 14 dpi, only minimal viral RNA load remained, and no replication competent virus was detected in the respiratory tract (Figure S2b – d). Lack of viral RNA in the blood of all animals suggested absence of systemic infection (data not shown).

Similar to previous observations (Gruber et al., 2020; Osterrieder et al., 2020), histopathology identified necrosuppurative bronchitis and bronchointerstitial pneumonia at 2 and 3 dpi, characterized by intrabronchial and intraalveolar infiltration by neutrophils and macrophages as well as severe, diffuse alveolar damage. Numbers and density of infiltrating immune cells, hyperplasia of bronchial and alveolar epithelial cells as well as alveolar and interstitial edema and endothelialitis peaked at 5 dpi. By 14 dpi, cellular influx into alveolar spaces was largely resolved, with fewer neutrophils, macrophages and lymphocytes observed within the interalveolar septa, while marked hyperplasia of alveolar epithelial cells remained (Figure S2e – n). Again, consistent with previous reports (Gruber et al., 2020; Osterrieder et al., 2020) no evidence of thrombotic events were observed.

To obtain a higher resolution of the tissue response, we performed scRNA-Seq at time points spanning early infection, peak inflammation and the resolution phase of viral pneumonia. Cell type clusters detected in lungs corresponding to leukocyte-subset-signatures included alveolar, interstitial, and monocytic macrophages, *Treml4*$^{+}$-monocytes, neutrophils, dendritic cells, B, T, and natural killer (NK) cells. We further identified typical resident cell types, including alveolar epithelial cells type 1 (AT1) and 2 (AT2), ciliated epithelial, endothelial, and smooth muscle cells, and fibroblasts (Figure 1a, S3a). By integrating scRNA-Seq-derived cell frequencies with manually counted cell numbers over time, we mapped the dynamics of infection-induced pulmonary leukocyte recruitment compared to uninfected animals (Figure 1b, c). Neutrophils were the first immune cells recruited to the lungs (peak at 2 dpi), closely followed by an influx of monocyte-derived macrophages (peak at 5 dpi). NK and T lymphocyte recruitment to lungs was first detected at 5 dpi and peaked at day 14

Figure 1

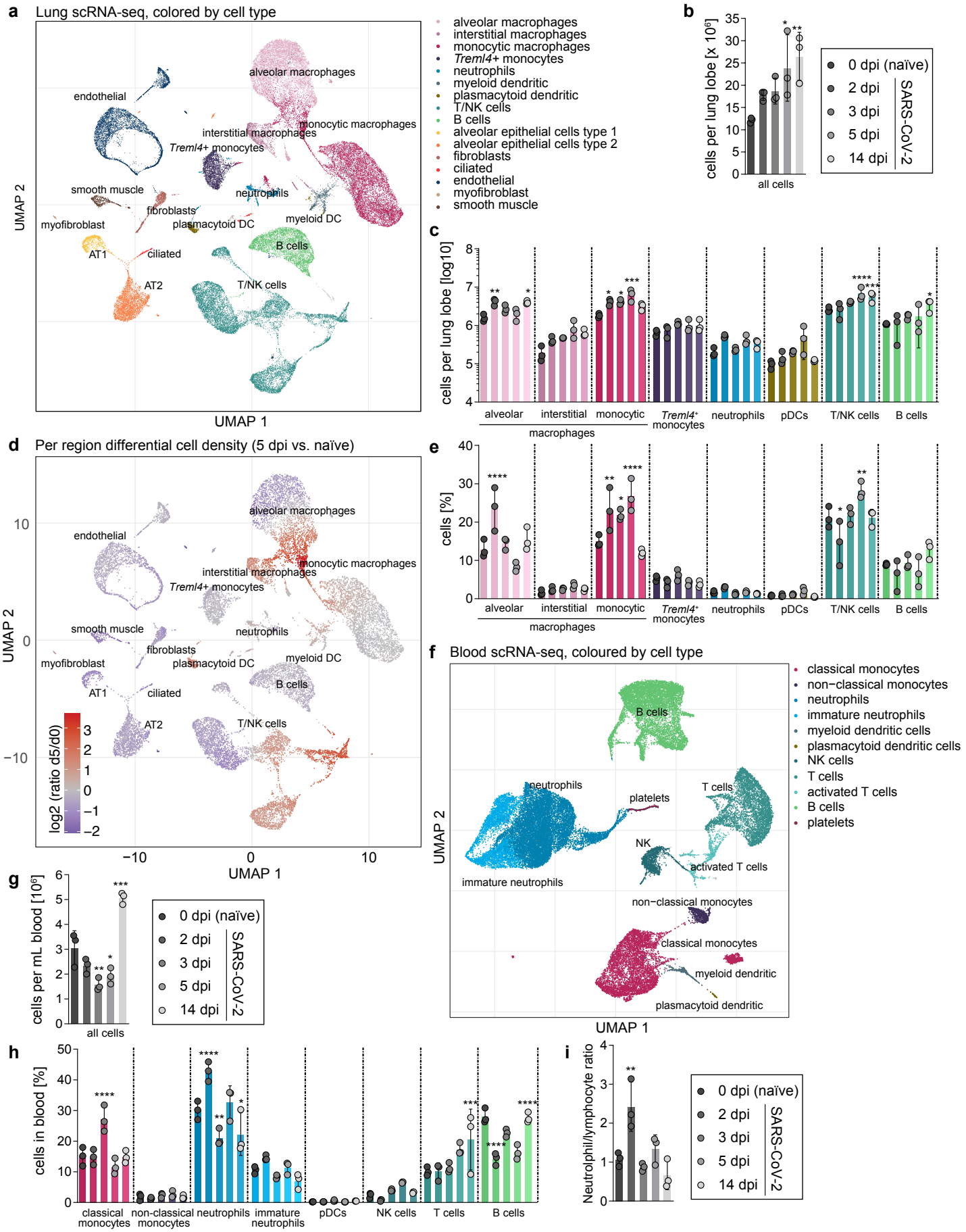

Figure 1: Single-cell dynamics in lungs and blood of SARS-CoV-2 infected Syrian hamsters

(a), UMAP plot of identified cell populations in Syrian hamster lungs. (b), Cell count of isolated cells per lung lobe over time (2, 3, 5 and 14 dpi) and control group (naïve, “d0”). (c), Count of hematopoietic cells per lung lobe in naïve hamsters and over time pi. (d), Changes in cellular density of lung cells in UMAP projection. Coloration indicates log2 fold change between control group and 5 dpi. (e), Percentage of hematopoietic cells per lung lobe in naïve hamsters and over time pi. (f), UMAP plot of identified cell populations in blood samples. (g), Cell count of isolated cells per mL blood in naïve hamsters and over time pi. (h), Percentage of identified cell populations in blood samples over time pi and naïve animals. (i), Neutrophil–lymphocyte ratio in blood samples over time pi and naïve animals. (a, d and f), Clusters defined by Louvain clustering, n = 3 per time point. (b, c, e, g, h and i), Data display means ± SD. n = 3 per time point. Ordinary one-way ANOVA, Sidak’s multiple comparisons test versus corresponding 0 dpi (naïve). * p < 0.05, ** p < 0.01, *** p < 0.001, **** p < 0.0001

(Figure 1c). The peak of lung inflammation on 5 dpi (Figure S2l) coincided with the highest proportion of inflammatory macrophages (monocytic macrophage cluster) and proliferating cytotoxic cells (T/ NK cell cluster) among lung cells (Figure S3b). Notably, despite pronounced neutrophilic bronchitis (Figure S2g), the overall neutrophil frequencies remained low. In line with histopathology, the peak of neutrophil recruitment was at 2 dpi, when neutrophil proportions presented ~3 % of all isolated lung cells (Figure 1e). In contrast, monocytic macrophages population at day 5 peaked at ~25 % of all lung cells (Figure 1d, e, S3b). Relative numbers of pulmonary tissue cell subsets fluctuated mildly during infection, declining proportionally as inflammatory cell influx rose at 2, 3 and 5 dpi (Figure S3c, d). At 14 dpi, increased numbers of AT2 pneumocytes matched histopathology observations of epithelial hyperplasia, indicating tissue repair (Figure S2i, k, S3c).

Analogously, we analyzed scRNA-Seq data from WBC populations, to study systemic responses evoked by pulmonary SARS-CoV-2 infection. Detected cell populations included neutrophils, monocytes, dendritic, NK, B and T cells and various subpopulations thereof (Figure 1f, S3e). Infected hamsters displayed significant leukopenia at 3 and 5 dpi, probably reflecting pulmonary leukocyte recruitment. By 14 dpi this trend was inverted and peripheral blood leukocyte numbers were significantly higher than in naïve animals (Figure 1g, S3f). Increased proportions of neutrophils at 2 dpi suggested inflammation-induced granulopoiesis, and increasing proportions of T cells at 14 dpi indicated their clonal expansion (Figure 1h, S3b). Notably, calculated neutrophil–lymphocyte ratios only transiently increased at 2 dpi to a minor extend, matching observations in humans with non-severe as opposed to severe COVID-19 (Lagunas-Rangel, 2020; Liu et al., 2020) (Figure 1i). Overall scRNA-Seq cell profiling substantially extended histopathology analysis in hamsters, by defining kinetics of innate and adaptive immune cell trafficking to lungs in greater detail.

Bulk transcriptomics, proteomics and single-cell RNA sequencing reveal activation of anti-SARS-CoV-2 pro-inflammatory immunity in hamsters

After evaluating immune cell dynamics in blood and lungs, we performed bulk RNA-sequencing of lungs and blood and matched proteomics of lungs and serum to gain insights into qualitative changes into transcriptome and proteome alterations of SARS-CoV-2-induced immune responses.

Figure 2

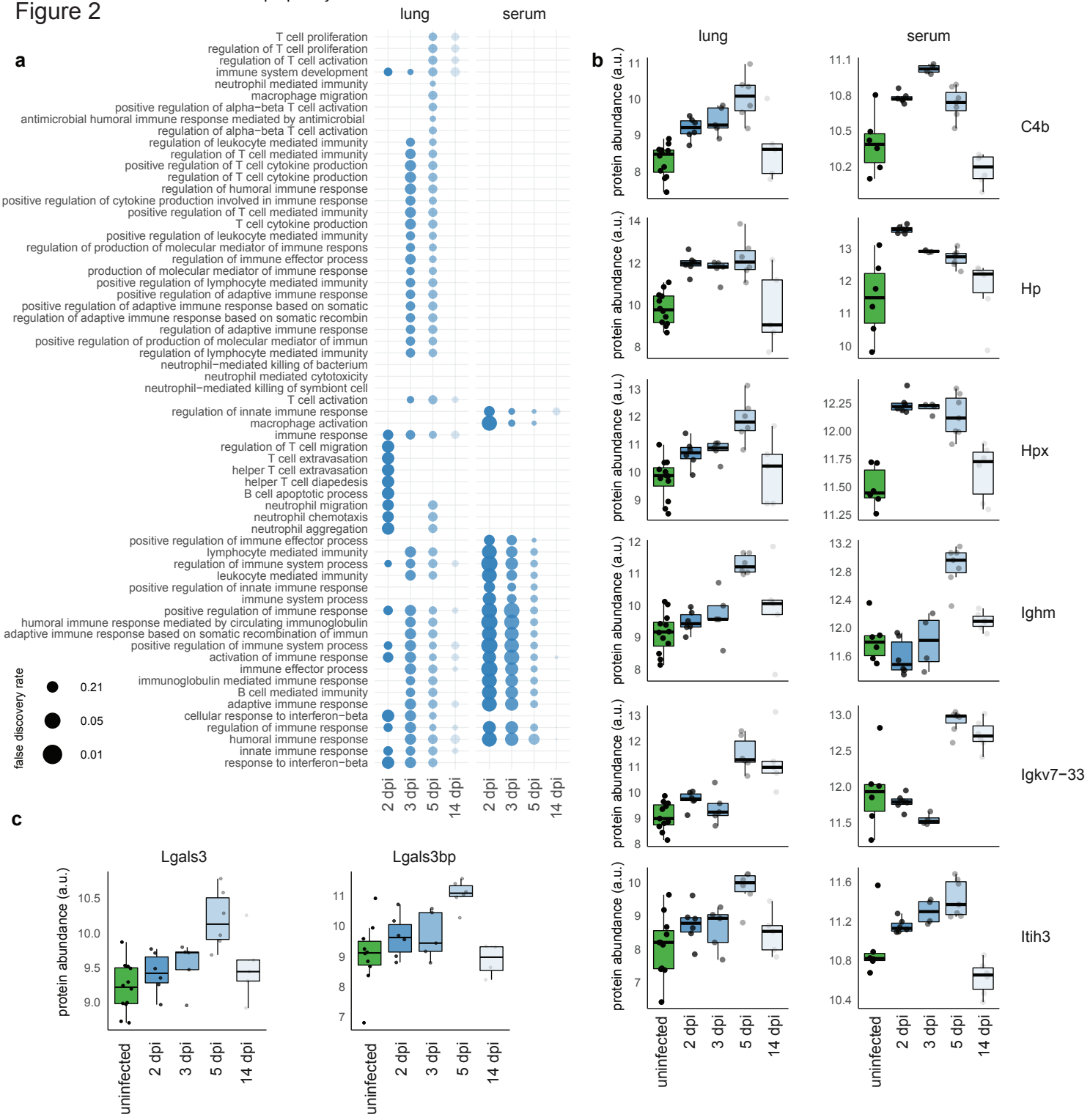

Figure 2: Proteomics analysis recapitulates transcriptomics and human COVID-19 patient data
(a), Temporal evolution of gene ontology/biological process terms connected with immune system response in lung tissue (left part) and in serum fluid (right part), for the indicated time points compared to samples from uninfected animals. Enriched terms were filtered for terms mentioning “immune”, “interferon”, “neutrophil”, “T cell” and “B cell”. Size of dots correspond to the inverse of the false discovery rate. (b), Expression values for differentially regulated proteins in hamster serum (control 3 dpi, p value < 0.01) and lung (control 5 dpi, p value < 0.01) that correlate with disease severity in human plasma. Controls from different days are plotted together. The thick line represents median of all values, lower and upper hinges correspond to medians of lower and upper half of set, respectively. Whiskers extend to a maximum of 1.5 times distance between first and third quartile. All values are shown. (c) Expression values for the differentially expressed proteins Lgals3 and Lgals3bp (only detected in lung samples).

Gene ontology (GO) enrichment analysis of the most differentially expressed genes in lungs and blood at 2, 3, 5 and 14 dpi versus naïve hamsters provided expected GO terms such as *defense response to virus*, *innate immune response,* and *cell activation* (Figure S4a, b). Pulmonary gene sets related to *type 1 interferon (IFN) signaling* correlated with presence of viral RNA, thus vanished by 14 dpi. Similarly, pulmonary gene sets related to *response to interferon-gamma (Ifng)* were highest at 5 dpi (Figure S4c). In blood, *type 1 IFN signaling* and *response to IFN-γ* gene sets were highest at 2 and 3 dpi (Figure S4d), perhaps reflecting recruitment of specific cells from blood to lungs. Overall, bulk RNA Seq identified an anti-viral immune response that was effectively resolved when the virus was cleared.

Proteome host response was in line with sequencing data, serum proteins peaked at 3 dpi and lung proteins at 5 dpi (Figure S4e). Agreement between bulk RNA sequencing and proteomics was highly consistent in lungs at 5 dpi ($r = 0.9$) (Figure S4f). Functional terms connected with immune response, such as innate and adaptive immunity, activation of complement system, humoral immune response and regulation of immune system processes were the most enriched in both lung and serum (Figure 2a). In lungs, the response to interferon-beta peaked at 3 dpi and stayed high until 5 dpi (Figure 2a). Most processes were resolved by 14 dpi.

We next aimed at comparing our data to published datasets from COVID-19 patients. In hamster serum, a total of 37 differentially expressed proteins were identified ($\alpha = 0.01$, providing FDR below 6 %), 17 compared to control and 31 proteins compared to 14 dpi when most effects are resolved. 20 of 31 proteins have been reported in human COVID-19 studies, 7 (Actg1, Apoa1, Apoc1, Gsn, Hp, Itih3, Lbp) of which correlate with disease severity (Messner et al., 2020b), all showing the same direction and a response at WHO 4 with the maximum amplitude at WHO grade 7 (Figure S4g).

In hamster lungs, at peak response (5 dpi) we identified 150 differentially expressed proteins. 13 differentially expressed proteins have been reported to be regulated in human plasma (Demichev et al., 2020b) with 9 showing the same trend (Table S2 for protein lists). Of these, 6 proteins (C4b, Hp, Hpx, Ighm, Igkv7-33, Itih3) are also changed in hamster serum (Figure 2b). Although a comparison to moderate disease in human lung tissue is not possible, 22 proteins are reported to be regulated in human BAL fluid of critically ill patients (Zeng et al., 2020). The few proteins showing opposite regulation to COVID-19 patients were confirmed by bulk sequencing. Five out of 7 conflicting responses, namely C4b, Hpx, Rbp4, Cfd, and Agt in hamster serum

Figure 3

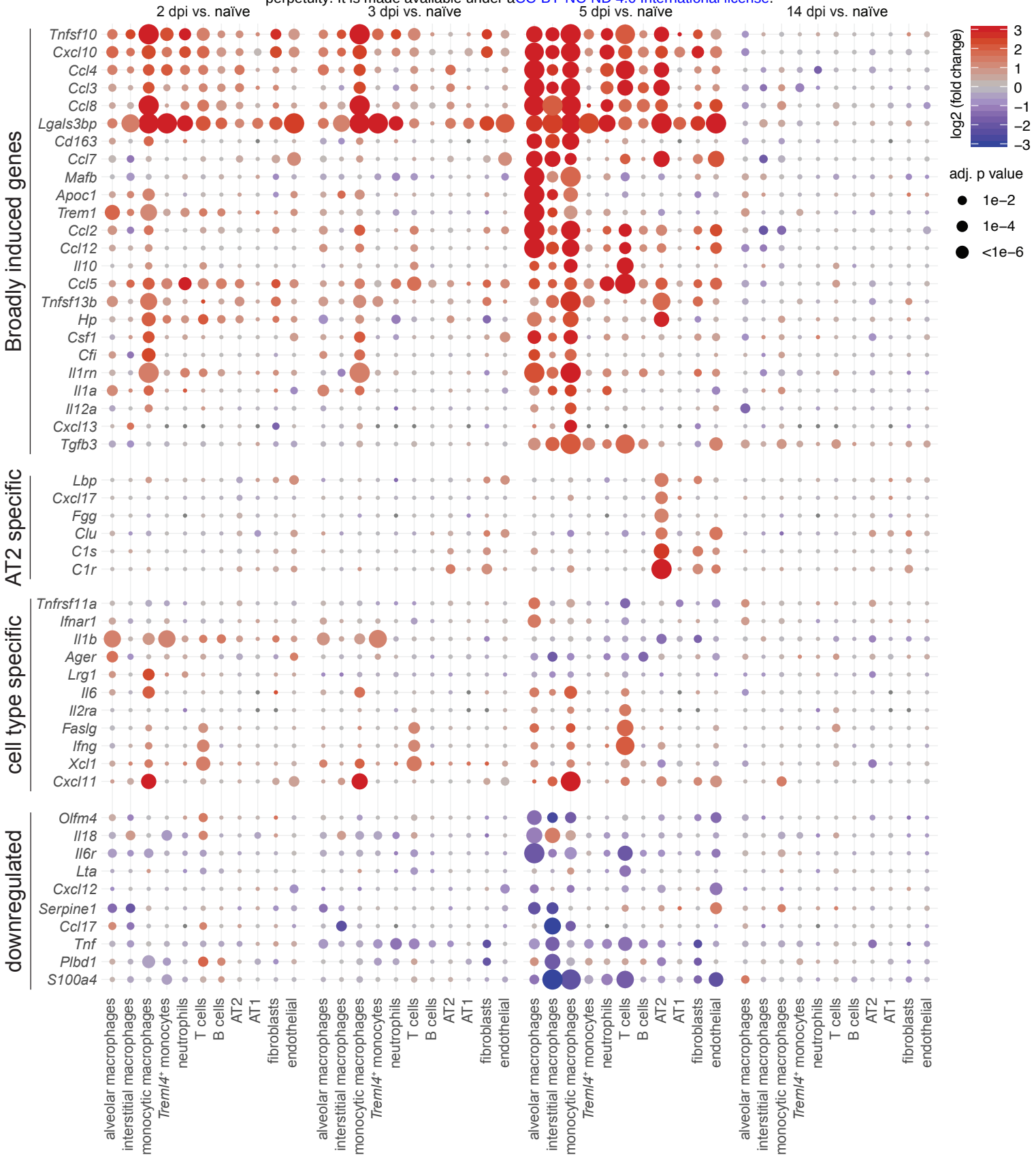

Figure 3: Induction of inflammatory mediators are strongest and earliest in myeloid cells
Dotplots of differentially expressed cytokines and inflammatory mediators in lungs. Shown are genes that display a significant absolute log2-transformed fold change of at least one in at least one comparison, and are grouped into four categories indicated on the left. Coloration and point size indicate log2-transformed fold changes and P values, respectively, of genes at 2 dpi relative to control groups (naïve). Adjusted P values were calculated by DEseq2 using Benjamini-Hochberg corrections of Wald test p values. Genes are ordered by unsupervised clustering, cell type as in Figure 1.

compared to human plasma as well as 8 out of 12 for hamster lung tissue compared to human BAL were confirmed.

Next, we refined our transcriptome analyses with the higher resolution of scRNA-Seq and related identified bulk GO terms to cell types, concentrating on inflammatory mediators in lungs and blood (Figure 3). Indeed, various pro-inflammatory chemokines were expressed by lung cells and showed distinct cellular and temporal expression patterns. Classical pro-inflammatory cytokines, e.g. *Il1a* and *Il1b* transcripts were elevated only early in infection at 2 and 3 dpi in alveolar and monocytic macrophages, and alveolar macrophages and *Triggering receptor expressed on myeloid cells-like 4* (*Treml4*)+ monocytes, respectively. By 5 dpi, AT2 cells showed a unique range of upregulated inflammatory mediators such as *Cxcl17*, *Lipopolysaccharide Binding Protein (Lbp)*, *fibrinogen gamma gene (Fgg)*, and *clusterin (Clu)*. Within the analysis in Figure 3 *galectin 3-binding protein* (*Lgals3bp*) gene stood out as being upregulated in many different cell types from 2 dpi to 5 dpi. Notably, we likewise measured increased levels of the Lgals3bp protein in lungs (Figure 2c), which was shown to be regulated also in plasma of COVID-19 patients and correlated with severity (Messner et al., 2020b).

Taken together, we identified clear changes in transcriptome, proteome and pro-inflammatory signatures on single-cell level in response to SARS-CoV-2 infection, displaying a highly active immune response that to large extents were described in COVID-19 patients underlying the validity of our model.

Migratory myeloid cells dominate pulmonary transcriptional response to SARS-CoV-2 infection in Syrian hamsters and COVID-19 patients

To pinpoint the individual role of the identified cells in anti-SARS-CoV-2 immunity, we analyzed the 15 - 20 most differently expressed genes in each cell subset. In the early stage of infection at 2 dpi, robust, local transcriptome changes were observed primarily in lung monocytic and interstitial macrophages, neutrophils and endothelial cells, whereas AT1 and AT2 epithelial cells and alveolar macrophages showed comparably little change in mRNA expression (Figure 4a).

A common set of anti-viral effector genes was found upregulated in many cell types (Schoggins, 2019). These include e.g. *interferon-stimulated gene 15* (*Isg15*), *MX dynamin like GTPase (Mx)1, Mx2, Interferon-induced protein with tetratricopeptide repeats 3* (*Ifit3),* and *Sp100*, as well as transcription factors, such as *Interferon*

Figure 4

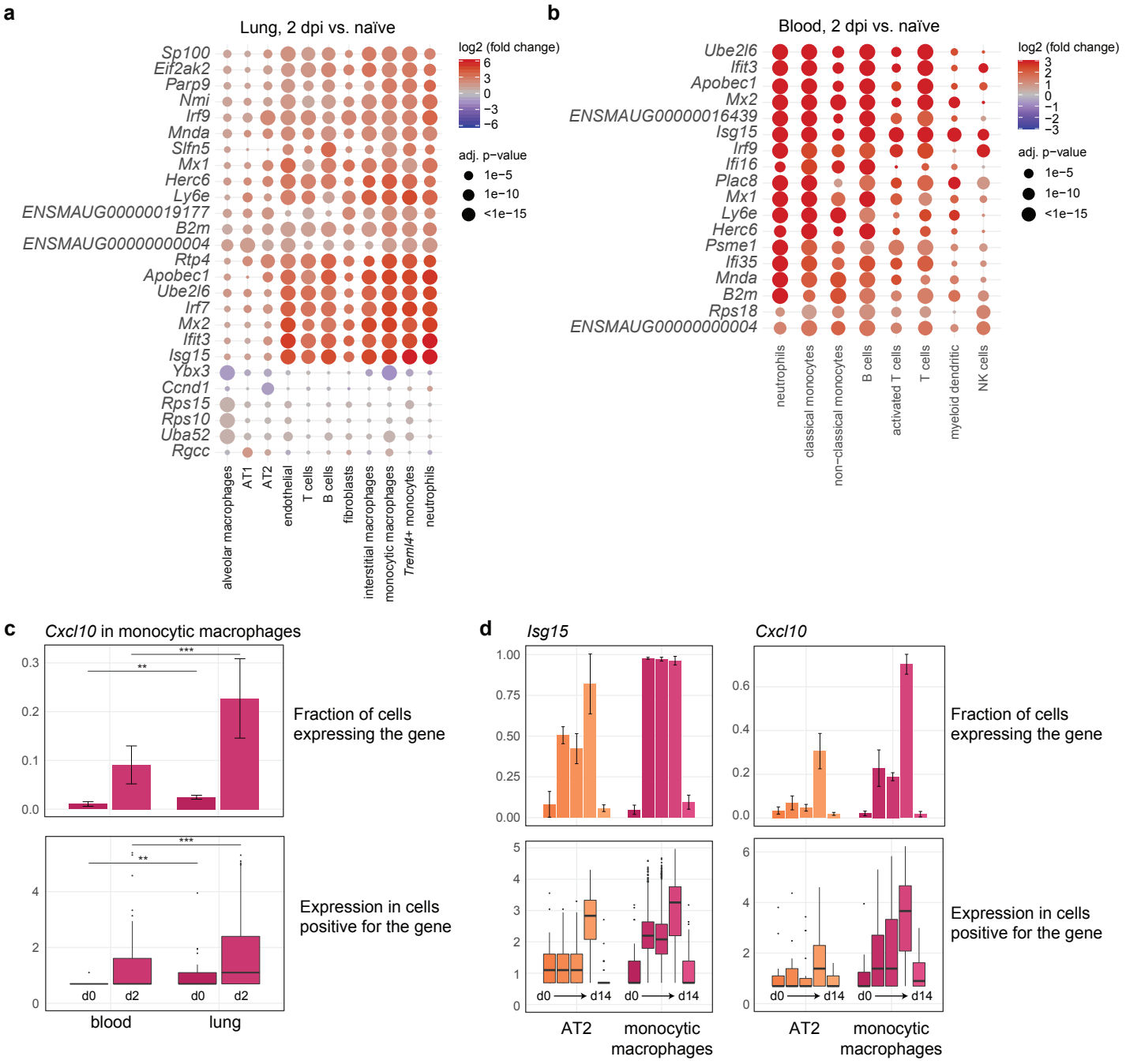

Figure 4: Transcriptional response to SARS-CoV-2 infection is strong in myeloid and moderate in epithelial cells (a, b), Dotplot of differentially expressed genes in lungs (a) and blood (b). Shown are genes that are in at least one cell type among the top 4 most changing genes as ranked by adjusted p value. Example: top 4 most changing genes in alveolar macrophages are *Ybx3*, *Rps15*, *Rps10*, and *Uba52*. Coloration and point size indicate log2-transformed fold changes and p values, respectively, of genes at 2 dpi relative to control groups (naïve). Adjusted p values were calculated by DEseq2 using Benjamini-Hochberg corrections of Wald test p values. Cell types and genes are ordered by unsupervised clustering. (c), Top, fraction of monocytic macrophages expressing *Cxcl10* in blood and lungs from naïve animals and 2 dpi. Bottom, boxplots of Cxcl10 gene expression values of cells positive for *Cxcl10* expression. Significance levels were calculated using generalized linear mixed-effects models for bar plot and a Wilcoxon rank sum test on all cells (i.e. not only the ones expressing the gene) for boxplots. * means p value 0.05-0.01, ** means p value 0.01-0.0001, *** means p value smaller 0.0001. See materials and methods for details. (d), As in (c), but only in lungs, all time points and both alveolar epithelial cells type 2 (AT2) and monocytic macrophages. Displayed are values for *Isg15* (left) and *Cxcl10* (right). For all bar plots, data display means ± SD, n = 3 per time point. For all boxplots, lower and upper hinges correspond to first and third quartiles. Whiskers extend to a maximum of 1.5 times the distance between first and third quartile. Outliers beyond are marked by single dots.

regulatory factor (*Irf) 7* and *Irf9* (Figure 4a, Figure S5a). Blood transcriptome analysis recapitulated this early transcriptional activity at 2 dpi (Figure 4b, Figure S5b), but declined by 5 dpi, whereas the signature persisted in the lungs until 14 dpi (Figure S5a, b). The genes that differed most between classical blood monocytes and their counterparts in the lungs encoded chemokines and activation markers, including *CXC chemokine ligand 10* (*Cxcl10)*, *Slamf9*, *Il18bp*, *Ifitm2*, *Ccl8*, *Ccl4* and *Ccl5* (Figure 4c, Figure S5c), indicating that activation and acquisition of effector function occurred in the lungs.

Although AT2 cells are a main target of SARS-CoV-2 in lungs (Hou et al., 2020), they displayed weaker and later transcriptional changes upon infection compared to monocytic macrophages (Figure 4a, d, S5a, d).

Notably, at 14 dpi differential transcriptional responses related to defense resolved in blood and lung cells. Instead, we observed upregulation of cell cycle proliferation genes in AT2 cells including *Marker of Proliferation Ki-67* (*Mki67*), *Ubiquitin-conjugating enzyme E2 C* (*Ube2c*), *Aurora B kinase* (*Aurkb*), and *Stathmin* (*Stmn1*) (Figure S5a). This transcriptome profile indicated initiation of a repair program by AT2 cells, proliferating to replace damaged AT1 cells (Olajuyin et al., 2019), and matching the increase in AT2 numbers and alveolar epithelial hyperplasia observed earlier (Figure S2, S3). Finally, we put our hamster lung scRNA-Seq data in context with BAL scRNA-Seq data from patients with moderate-to-severe COVID-19 (Liao et al., 2020) and healthy controls (Morse et al., 2019). As in the hamster data, we observed stronger transcriptional responses in macrophages compared to epithelial cells (Figure S5e). Furthermore, the upregulated gene program containing e. g. *CXCL10*, *CCL2* or *CCL8* was substantially overlapping (Figure S5f).

To test whether hamster tissue responses are representative of infected human epithelial cells, we next referred to our scRNA-Seq dataset derived from nasopharyngeal swabs of 19 COVID-19 patients and 5 healthy controls (Chua et al., 2020). Here again, human and hamster epithelial cells derived from infected individuals and animals, respectively, showed a similar, moderate induction of most inflammatory mediators (Figure S6a, b). As notable difference, the strong induction of neutrophil-recruiting chemokines targeting CXC chemokine receptor (CXCR) 2, such as *CXCL1*, *CXCL3*, *CXCL6* and *CXCL8,* were found only in human basal and secretory cells with severe COVID-19 but were absent in moderately ill Syrian hamsters (Figure S6a, Figure 3). Aside from the epithelial inductions of neutrophil-attractant transcripts unique

to severe COVID-19, SARS-CoV-2 infected hamsters and patients displayed strikingly similar pro-inflammatory immune profiles specifically in migratory myeloid cells.

Early activation of TLR/NF-kB dependent transcription of pro-inflammatory cytokines in monocytic macrophages by SARS-CoV-2 infection

Next, we asked whether the observed cellular transcriptional response to SARS-CoV-2 infection was directly or indirectly influenced by the presence of virus in each cell type. First, we determined the fractions of cells expressing SARS-CoV-2 entry receptors, *Angiotensin-converting enzyme 2* (*Ace2) and transmembrane serine protease 2* (*Tmprss2)*, putative alternative receptors, *Basigin (Bsg)* and *Furin,* and cofactors, such as neuropilins (*Nrp1*), and heparan sulfate (*exostosin-1*, *Ext1)*) (Cantuti-Castelvetri et al., 2020; Daly et al., 2020; Davies et al., 2020) in hamster lungs (Figure 5a, Table S3). Ciliated epithelial cells most frequently expressed *Ace2* (~4 – 22 %), as did a smaller proportion of AT2 cells (~3 – 5 %) (Table S3). By in situ-hybridization, we visualized SARS-CoV-2 RNA in bronchial epithelial cells (Figure 5b), and alveolar epithelial cells morphologically consistent with both type I (Figure 5c, arrowhead) and type II (Figure 5c, arrow) cells, whereas endothelial cells were consistently devoid of virus (Figure 5b, hash). Importantly, viral RNA was detected in high numbers of intrabronchial and intraalveolar macrophages (Figure 5d, arrows) at early time points. A fraction of macrophages contained high loads of virus without cell debris, pointing towards uptake of cell-free virus (Figure 5d, inset). For comparison, a section of alveoli from uninfected hamsters is shown (Figure 5e).

In accordance with *in situ*-hybridization data, scRNA-Seq data revealed that most viral RNA content was found in monocytic macrophages, and not in epithelial cells (Figure 5f, Table S3). For epithelial and endothelial cells, frequencies of virus-positive cells were highest at 3 dpi, declining by 5 dpi to become absent at 14 dpi, indicating removal of virus-containing cells (Table S3). In contrast, alveolar macrophages showed highest viral loads at 5 dpi (~25 %), paralleling decline of virus-positive tissue cells, thus pointing towards potential increase in phagocytic activities (Table S3). To further investigate how cell-specific gene expression is modulated by the cell-associated viral RNA, we tested the correlation between gene expression and viral load in monocytic macrophages.

We first compared gene expression levels in monocytic macrophages that did (vRNA(+)), or did not (vRNA(-)) contain viral RNA (Figure 5g, S7a). This revealed a set

Figure 5

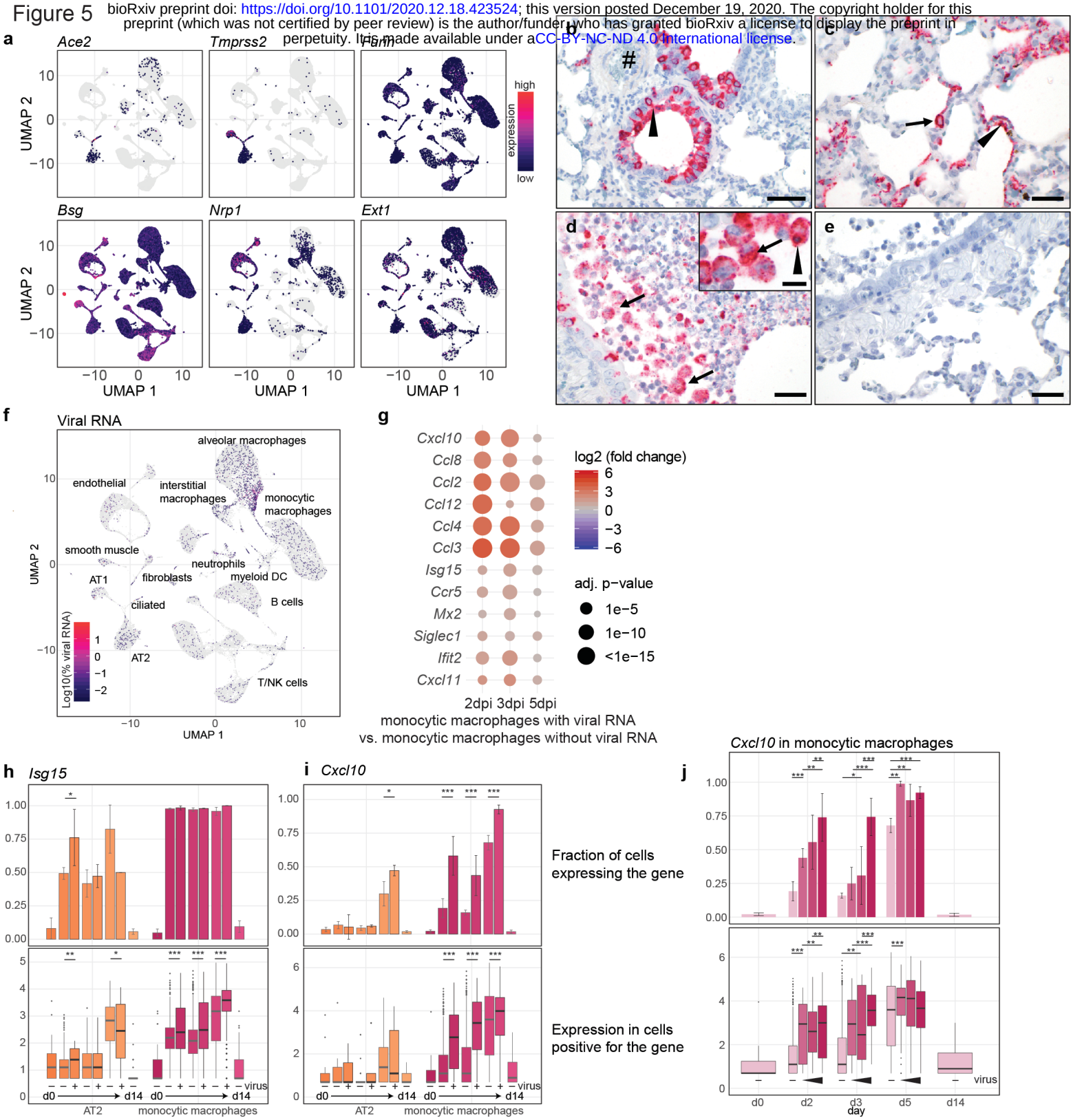

Figure 5: Virus RNA in monocytic macrophages leads to dose-dependent activation of pro-inflammatory cytokines by TLR signaling

(a), Feature plots of entry factor expression in UMAP projection. Coloration indicates expression values of indicated genes. (b-e), Detection of viral RNA by in situ-hybridization. Labeled are supposed endothelium (b, hash), bronchial epithelial cells (b, arrowhead), AT1 (c, arrowhead) and AT2 (c, arrow). (d, inset), macrophages containing viral RNA and cell debris (arrowhead), and an example of high levels of viral RNA without cell debris in the inset (arrow). For (b-e), red signals viral RNA and blue hemalaun counterstain. Time points: (b-c) from 2 dpi, (d) from 3 dpi, (e) from naïve. Bars: (b, d, e) = 50 µm, (c) = 100 µm, Inset in (c) = 20 µm. (f), Cells in the UMAP projection are colored by amount of viral RNA (log10 transformed percentage of viral RNA per cell), along with overview of identified cell types in lungs. (g), Dotplot of cytokine expression in monocytic macrophages containing viral RNA compared to those without viral RNA. Coloration and point size indicate log2 fold change and P value for each time point 2, 3 and 5 dpi. (h, i), Box- and barplots of *Isg15* (h) and *Cxcl10* (i) gene expression in AT2 and monocytic macrophages along, comparing cells containing viral RNA to those without for 2, 3, and 5 dpi. Barplot shows percentage of cells positive for respective gene, with mean ±SD, n = 3. Boxplots show gene expression levels in cells positive for respective gene. (j), Box- and barplots of *Cxcl10* in monocytic macrophages and fraction of *Cxcl10* positive cells for each time point pi and naïve animals, with cells grouped by increasing virus levels for 2, 3, and 5 dpi. (e and f), for barplots, data display means ± SD. Significance levels calculated using generalized linear mixed-effects models for barplot and a wilcoxon rank sum test on all cells (i.e. not only the ones expressing the gene) for boxplots. * means p value 0.05-0.01, ** means p value 0.01-0.0001, *** means p value smaller 0.0001.

of genes that were present at much higher levels in vRNA(+) monocytic macrophages at the earlier time points (2 dpi, 3 dpi), but not at 5 dpi (Figure S7a). Gene ontology and KEGG pathway analysis showed that this gene set is enriched for Toll-like receptor (TLR) signaling (Figure S7b). Specifically, this gene set contained a range of pro-inflammatory cytokines such as *Cxcl10* or *Ccl2* (Figure 5g), which are activated by the NF-kB pathway downstream of TLRs (Liu et al., 2017). On the other side, expression levels of NF-kB independent ISGs such as *Isg15* or *Mx2,* induced by interferons or cytosolic RNA sensors (Schneider et al., 2014), were only slightly more elevated in vRNA(+) compared to vRNA(-) monocytic macrophages (Figure 5g).

We therefore investigated expression of *Isg15* and *Cxcl10* in monocytic macrophages in more detail, and in comparison to AT2 cells (Figure 5h, i). In AT2 cells, *Isg15* expression was induced in about 50 percent of the cells at 2 dpi, with the gene being present (Figure 5h, upper panel) and expressed at somewhat higher levels in vRNA(+) cells. In monocytic macrophages however, *Isg15* was expressed in all cells, and at slightly elevated levels in vRNA(+) cells. In comparison, *Cxcl10* was barely present in AT2 cells at 2 dpi and 3 dpi (Figure 5i). On the other hand, monocytic macrophages start to express *Cxcl10* already at 2 dpi, and much stronger so the vRNA(+) cells (Figure 5i). At 5 dpi, the difference between vRNA(-) and vRNA(+) monocytic macrophages becomes smaller, but is still significant (Figure 5i).

We further analyzed the dose-dependency of this transcriptional response to virus uptake in monocytic macrophages. Cells were binned in three groups of equal size with increasing content of viral RNA (Figure 5j). We found that at earlier time points (2 and 3 dpi), but not a 5 dpi, cells with higher amounts of viral RNA-signal, also expressed more *Cxcl10* (Figure 5j). Overall, this indicates that viral RNA in monocytic macrophages induces early, strong activation of dose-dependent virus sensing, leading to a substantial increase of NF-kB-regulated pro-inflammatory chemokines.

At 5 dpi, broad inflammation likely masks direct viral RNA-triggered responses by activating the expression of pro-inflammatory genes in vRNA(+) and vRNA(-) cells equally. In contrast, AT2 cells, supposed primary site of viral replication, show by far less activation of both NF-kB dependent and independent transcriptional responses as compared to monocytic macrophages.

Endothelial cells participate in anti-viral and pro-inflammatory responses

Having observed vast similarities of human and Syrian hamster immune responses in moderate SARS-CoV-2 infection on transcriptomic and proteomic levels, we next turned our attention to dissection of the molecular mechanisms in lung tissue compartments that have so far not been assessed longitudinally in moderate COVID-19 patients, since invasive tissue sampling is hardly possible.

Endothelial cells likely participate in COVID-19 pathogenesis (Ackermann et al., 2020; Michalick et al., 2020), but little is known about the dynamics of their response to inflammation *in vivo*. Subclustering of cells of endothelial origin identified endothelial cells of lymphatic and bronchial vasculature, pulmonary arteries, pulmonary capillaries and pulmonary veins with unique features (Figure 6a, Figure S8a, b). Interestingly, bronchial endothelial cells, pulmonary artery and capillary endothelial cells all displayed strong and early anti-viral gene expression profiles at 2 dpi (Figure 6b). Pulmonary arterial endothelial cells responded most rapidly to infection, with high expression of *Cxcl10*, *Tnfsf10*, and *Ccl7* by 2 dpi (Figure 6c). Responses of bronchial vasculature, pulmonary capillary and pulmonary vein endothelial cells were similar but delayed, peaking at 5 dpi. In addition to the distinct temporal dynamics of endothelial activation in different tissues, we observed a spatial regulation of expression of monocyte and effector T cells attractants. Pulmonary artery and vein endothelial cells preferentially transcribed *Ccl7*, a chemoattractant binding multiple CC receptors, including CCR1, CCR2, CCR3, CCR5, and CCR10 (Ford et al., 2018). Pulmonary capillary endothelial cells, however, preferentially expressed the pleiotropic *Ccl8*, binding at least CCR2, CCR3 and CCR5 (Blaszczyk et al., 2000), while bronchial vasculature endothelial cells were characterized by *Ccl2* (Figure 6c). ICAM-1 and VCAM-1 upregulation, expressed by endothelial cells following inflammatory stimuli to allow for leukocyte transmigration (Schnoor et al., 2015), was highest in bronchial endothelial cells and pulmonary artery cells at 5 dpi, corresponding with the influx of T cells revealed by scRNA-Seq data (Figure 6c). Overall lung endothelial cells shared an anti-viral gene profile but revealed distinct patterns of chemokines targeting primarily monocytes and Th1 cells. Unlike cells of epithelial origin, endothelial cells failed to show evidence of proliferation and cell cycle activity that could have indicated their participation in tissue repair processes during the study period (*DNA topoisomerase 2-alpha* (*Top2a*), *Mki67*, *Ube2c*) (Figure 6c).

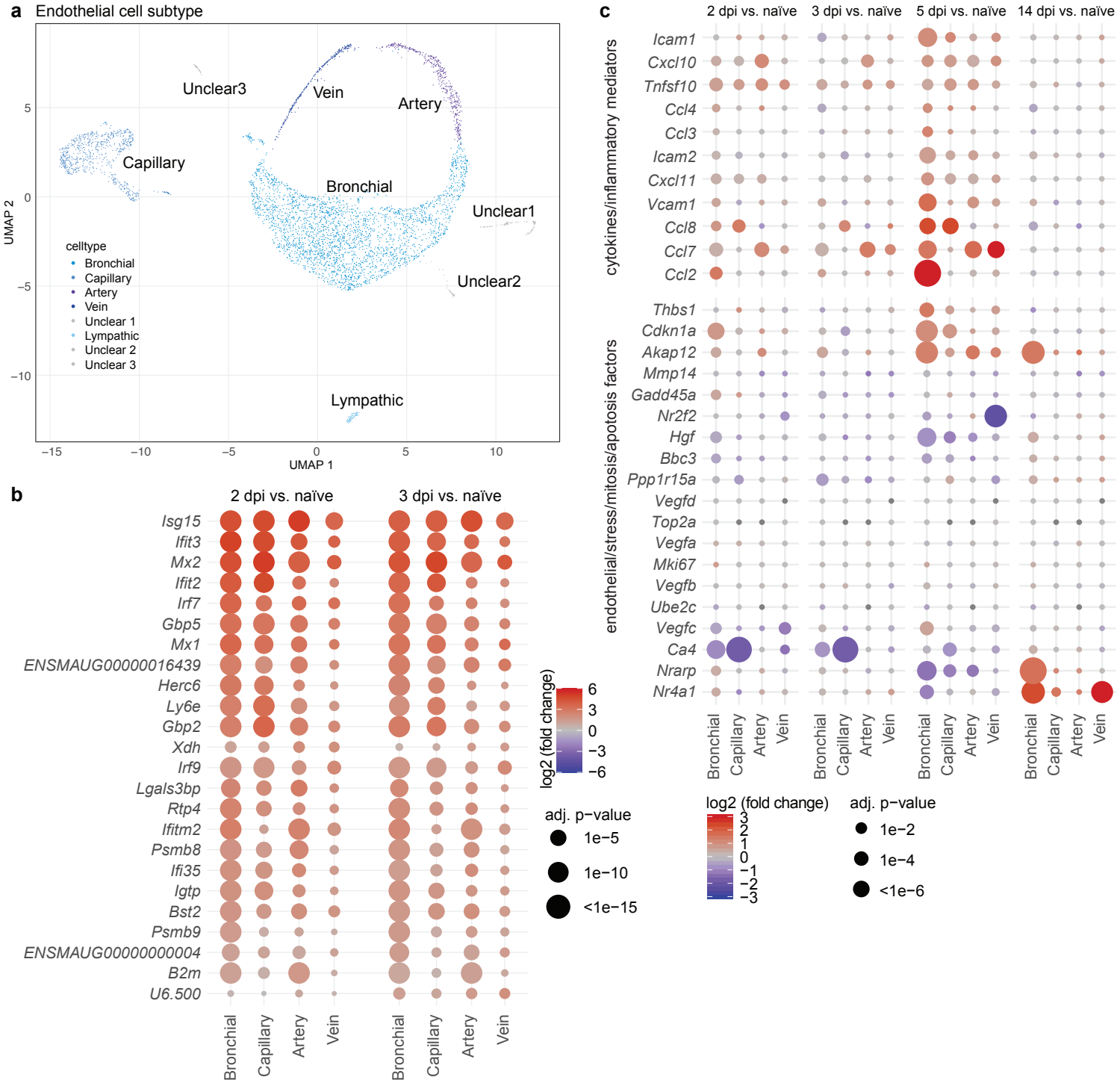

Figure 6: Endothelial cells show subtype and time specific activation of cytokines
(a), UMAP plot of lung endothelial cell subpopulations. (b), Dotplot of differentially expressed genes in lung endothelial cell subpopulations over time. Shown are genes that are in at least one cell type among the top 10 most changing genes as ranked by adjusted p value. (c), Dotplot of differentially expressed genes from two curated sets as indicated in lung endothelial cell subpopulations over time pi. For both (b) and (c), coloration and point size indicate log2-transformed fold changes and P values, respectively, of genes at 2 dpi relative to control groups (naïve). Adjusted p values were calculated by DEseq2 using Benjamini-Hochberg corrections of Wald test p values.

Type 1 effector T cells are efficiently recruited to lungs in SARS-CoV2 infection

Our initial cellular analysis of scRNA-Seq data from lung samples had grouped T and NK cells in one set of connected clusters, and we had observed their significant increase in lungs at 5 and 14 dpi (Figure 1). We hypothesized that cytotoxic immunity might be linked to viral clearance observed at 5 dpi, and elimination by 14 dpi (Figure S2). Therefore, we subclustered NK and T cells to identify 4 subpopulations based on *Cd3e*, *Cd4*, *Cd8a* and *Natural Killer Cell Granule Protein 7* (*Nkg7)* gene expression (Figure 7a, S9a), CD4$^+$ T cells (*Cd3e*$^+$*Cd4*$^+$), CD8$^+$ T cells (*Cd3e*$^+$*Cd8a*$^+$), NK cells (*Cd3e*$^-$*Nkg7*$^+$) and innate lymphoid-(ILC) like cells (*Cd3e*$^-$*Cd4*$^-$*Cd8a*$^-$*Nkg7*$^-$). CD4$^+$ T, CD8$^+$ T and NK cell numbers increased with infection time and peaked at 5 dpi (Figure 7b). SARS-CoV-2 infection initiated type 1 immunity and cytotoxic effector mechanisms in lungs (Figure 7c, S9b). The fraction of NK cells expressing interferon gamma (*Ifng*) increased significantly at 2 dpi and peaked at 3 dpi (Figure 7d, left). In contrast, *Ifng*$^+$ effector T cells (*Ifng*$^+$ CD4$^+$ and CD8$^+$ T cells) peaked at 5 dpi (Figure 7d, right). By 14 dpi, both *Ifng*$^+$ NK and T cell responses had declined to naïve levels (Figure 7d).

NK cells and CD8$^+$ T cells expressed high levels of cytotoxic genes, but upregulation of *Gzma* was highest in CD4$^+$ T cells (Figure 7c, S9b). Cytotoxic effector function of T cells was evident, 60 % of all CD4$^+$ T and 70 % of all CD8$^+$ T expressed *Gzma* at 5 dpi (Figure 7e). Furthermore, we detected “cells” carrying both a specific cell type marker (for AT1 / AT2 / endothelial cells, or monocytic macrophages), and simultaneously the cytotoxic cell marker *Gzma*. These possible doublets were absent in naïve animals and appeared particularly and reproducibly for endothelial and AT1 cells at the peak of effector T cell recruitment 5 dpi (Figure 7f), indicating possibly either killer-target interaction or more likely T cell transmigration. The latter notion was supported by the strong immigration of lymphocytes in the endothelium observed in histopathology (Figure 7g).

Induction of high-affinity neutralizing antibodies is the primary aim of most vaccination strategies against viruses. In the here described primary infection with SARS-CoV-2, neutralizing antibodies were evident by 5 dpi and declined mildly until 14 dpi (Figure 7h). Matching course of mu chain protein levels measured by proteomics (Ighm, Figure 2b). Along with cytotoxic CD8$^+$ T cells, we found pronounced recruitment of CD4$^+$ Th1 cells expressing *Ifng*, neutralizing antibodies reached relevant numbers only by 14 dpi

Figure 7

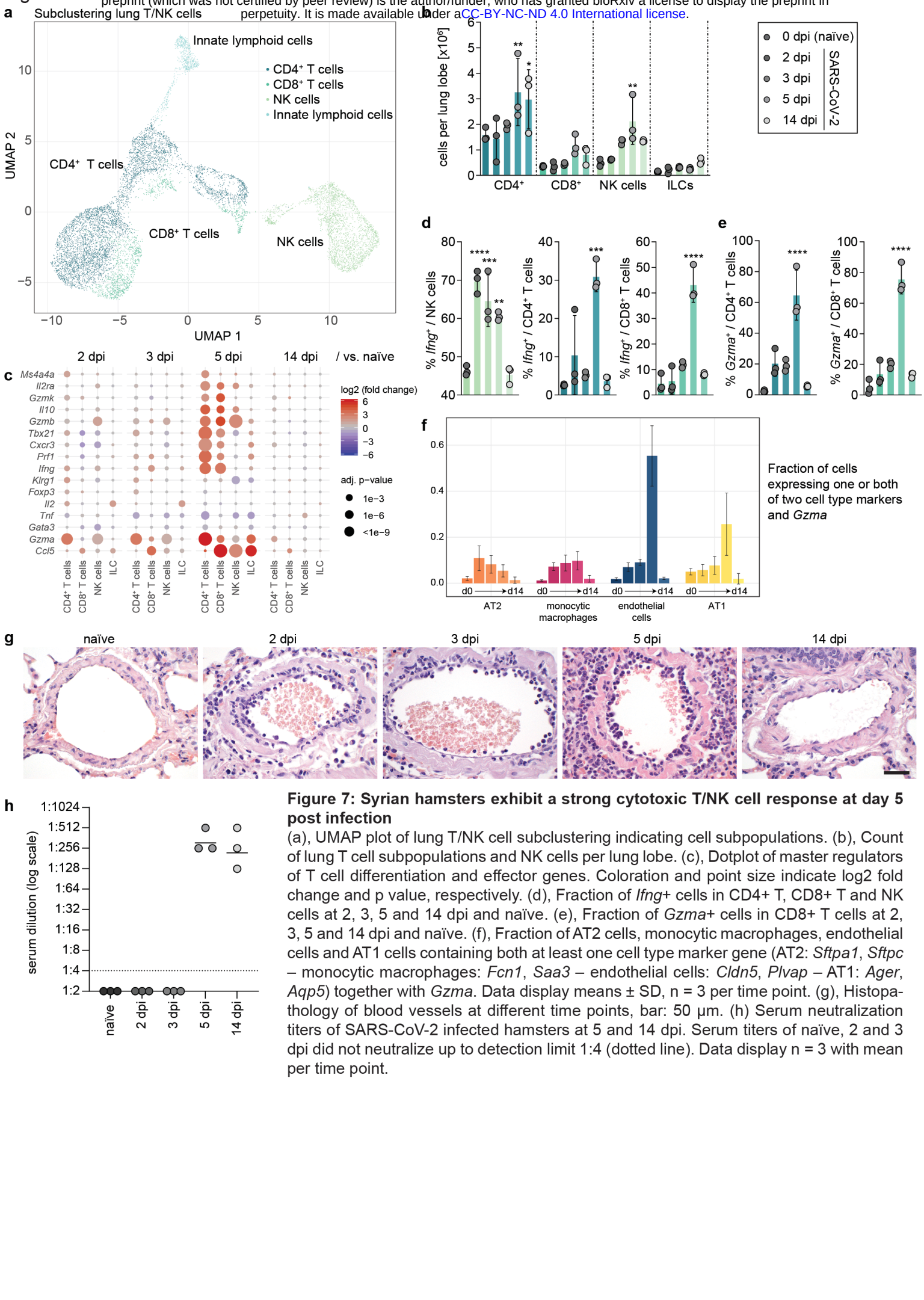

Figure 7: Syrian hamsters exhibit a strong cytotoxic T/NK cell response at day 5 post infection

(a), UMAP plot of lung T/NK cell subclustering indicating cell subpopulations. (b), Count of lung T cell subpopulations and NK cells per lung lobe. (c), Dotplot of master regulators of T cell differentiation and effector genes. Coloration and point size indicate log2 fold change and p value, respectively. (d), Fraction of *Ifng*+ cells in CD4+ T, CD8+ T and NK cells at 2, 3, 5 and 14 dpi and naïve. (e), Fraction of *Gzma*+ cells in CD8+ T cells at 2, 3, 5 and 14 dpi and naïve. (f), Fraction of AT2 cells, monocytic macrophages, endothelial cells and AT1 cells containing both at least one cell type marker gene (AT2: *Sftpa1*, *Sftpc* – monocytic macrophages: *Fcn1*, *Saa3* – endothelial cells: *Cldn5*, *Plvap* – AT1: *Ager*, *Aqp5*) together with *Gzma*. Data display means ± SD, n = 3 per time point. (g), Histopathology of blood vessels at different time points, bar: 50 µm. (h) Serum neutralization titers of SARS-CoV-2 infected hamsters at 5 and 14 dpi. Serum titers of naïve, 2 and 3 dpi did not neutralize up to detection limit 1:4 (dotted line). Data display n = 3 with mean per time point.

– thus, the peak of T cells corresponded with a vanishing virus responses, indicating successful cellular effector programs.

Discussion

Detailed understanding of COVID-19 pathophysiology is imperative for the development of therapies to reduce numbers of patients developing lung injury. Notably, recent patient-centered research on COVID-19 was compromised by three blind spots: (i) Biomaterial is usually sampled after hospital admission, therefore the early phase of infection and host response has rarely been investigated. (ii) the BAL procedure to access the alveolar compartment is too dangerous for non-intubated patients with COVID-19 pneumonia, so that alveolar host responses can hardly be investigated in mild and moderate COVID-19. (iii) Lung tissue can exclusively be harvested after death in COVID-19 patients, precluding from investigations of non-myeloid alveolar or endothelial host responses in early disease, and enabling for analysis of later disease stadium only in case of fatal outcome. Thus, we performed in-depth analysis of the full course of moderate, self-limited disease that develops in SARS-CoV-2 infected Syrian hamsters. In this model, lungs are fully accessible, providing for detailed analysis of myeloid and non-myeloid compartments including vascular endothelium. Yet, while the immune response is qualitatively similar between human and hamsters in central aspects, the viral dose applied in experimental infections is likely to be higher than in natural aerosol infection. Consequently, infection kinetics, viral decay rate and immune responses are accelerated (Johansen et al., 2020; Khoury et al., 2020). In line, we observed the pulmonary peak of viral load, inflammation and cellular response between 3 and 5 dpi, whereas at 14 dpi the infection was resolved and mechanisms of tissue regeneration were induced. This course of disease confirms observations in other animal models including non-human primates.

Syrian hamsters developed rapid, but moderate, neutrophil recruitment predominantly to bronchi and lung parenchyma, which resolved by 3 dpi. We also observed little of the typical neutrophil-dependent alveolar damage. Although single-cell RNA-sequencing analysis likely underestimates the numbers of this fragile cell type (10x Genomics, 2020), these findings suggest a minor role for neutrophils. Nonetheless, the neutrophil response is noteworthy, as many other respiratory viruses, e.g. Influenza A Virus and MERS Virus, initiate little or no neutrophil trafficking in rodents (Dietert et al.,

2017). In fact, blood N/L ratios in COVID-19 patients were reported as markers for disease severity, and neutrophil extracellular traps as well as reactive oxygen species are suspected to contribute to adverse vascular events (Fu et al., 2020; Middleton et al., 2020). Confirming our classification of hamsters as a moderate disease model, N/L ratios were only mildly elevated at 2 dpi, and gene signatures of dysfunctional immunosuppressive neutrophils were observed in severe COVID-19 patients (Schulte-Schrepping et al., 2020), but not in Syrian hamsters.

In line with COVID-19 patient reports, alveolar macrophage numbers did not decrease in moderate disease settings (Liao et al., 2020), and monocytic macrophages were the largest cell population recruited to the lungs, with notable recruitment from 2 dpi on, and peak presence at 5 dpi (Chua et al., 2020; Schulte-Schrepping et al., 2020). Monocyte trafficking to lungs was initiated by local expression of CCR2 ligands, and endogenous chemokine expression served as a feedforward loop. Consequently, macrophages were the predominant inflammatory cell type in alveolar spaces as identified by histopathology. Moreover, macrophages presented the earliest and strongest transcriptional response to the infection, primarily responding to intracellular viral RNA with pro-inflammatory cytokines such as CXCL10, CCL2 and others. Notably, the monocytic macrophage pro-inflammatory expression profile was rather productive than dysregulated as it tended more towards effector T cell recruiting chemokines targeting CXCR3 and CCR5, and less towards pro-inflammatory cytokine expression. This matches observations on moderate versus severe courses of COVID-19 in patients and stands in contrast to findings in animal models with severe disease progression such as K18-hACE2 mice (Liao et al., 2020; Winkler et al., 2020). It seems unlikely that intracellular viral RNA found in macrophages is the result of active infection of these cells, as they have been demonstrated to be largely resistant to infection *ex vivo* (Hönzke et al., 2020) (Hönzke, personal communications). scRNA-Seq data obtained from African green monkeys infected with SARS-CoV-2 likewise did not support virus replication in macrophages (Speranza et al., 2020). Instead, virus uptake may derive from complement receptor and Fc receptor-mediated phagocytosis of complement and antibody-labeled virus, as suggested by neutralizing antibody titers at 5 dpi (Van Strijp et al., 1989). Further, we observed early increase in complement factors and IgM mu chain by proteomics analysis in lung tissue. Taken together, the Syrian hamster model endorses the hypothesis that monocyte-derived macrophages are a primary source of the strong pro-inflammatory response observed in COVID-19,

yet highlights that their presence not necessarily results in fatal outcome (Merad and Martin, 2020).

Presumably, SARS-CoV-2 primarily infects AT2 cells (Hou et al., 2020). Of note, only few of them were infected and they reacted with only marginal transcriptional responses, which is probably explained by the recent observation in human lungs that less than 10% of AT2 cells express the crucial entry receptor ACE2 (Hönzke et al., 2020). Moreover, coronaviruses are endowed with a multitude of mechanisms that block immunological cascades downstream of interferon signaling and cytoplasmic RNA sensing (V'Kovski et al., 2020). Only a small subset of *in vitro* highly infected cells express pro-inflammatory genes (Fiege et al., 2020; Wyler et al., 2020). Thus, despite being the primary target for viral replication, epithelial cells were not accountable for early systemic propagation of anti-viral or pro-inflammatory signatures.

Endothelial barrier dysfunction, resulting from endothelial cell stress or death, evokes lung edema and thus contributes to lung failure in severe COVID-19 (Ackermann et al., 2020; Escher et al., 2020; Marchetti, 2020; Thompson et al., 2017). However, mechanisms driving endothelial barrier failure in COVID-19 are not well understood, as the endothelial compartment is not accessible in living humans suffering from COVID-19. Autopsy studies reported presence of viral particles in human endothelial cells (Ackermann et al., 2020), but infection of endothelial cells by SARS-CoV has been questioned (To and Lo, 2004). In SARS-CoV-2 infected non-human primates viral infection of endothelial cells was not observed (Speranza et al., 2020). Here, we found that endothelial cells showed a rapid and strong induction of anti-viral response genes, but considering the absence of histopathological evidence for intraendothelial virus, we speculate that virus-positive endothelial cells found by scRNA-Seq were not infected, but were rather an artifact originating from contact with ambient virus or its RNA (Gruber et al., 2020; Osterrieder et al., 2020). Concomitant cellular and molecular inflammatory responses in blood suggested that systemic responses were additive to direct, local endothelial cell activation. Notably, this observation is in line with our recent findings that virus-free plasma of COVID-19 patients induced significant endothelial gap formation and loss of junctional VE-cadherin in human endothelial monolayers and lung tissue (Michalick et al., 2020). Endothelialitis, as observed in autopsies of deceased COVID-19 patients, was also found in infected hamsters (Gruber et al., 2020; Osterrieder et al., 2020) and corresponded to their transcriptional pro-inflammatory chemokine responses (Ackermann et al., 2020). Histopathological

552 evidence of pronounced lymphocyte trafficking via capillary endothelial cells also
553 correlated with endothelial *Ccl8* expression.
554 Lymphocyte recruitment in response to CXCR3 and CCR5 targeting chemokines
555 resulted in the presence of $CD4^+$ and $CD8^+$ T cells with cytotoxic expression pattern in
556 lungs starting at 3 dpi. Most importantly, viral clearance coincided with appearance of
557 effector T and NK cells stressing their relevance for resolution of SARS-CoV-2 infection
558 and highlighting their importance in vaccination strategies. Studies from other
559 coronaviruses suggest that type 1 immunity is the primary mechanism controlling the
560 infection (Janice Oh et al., 2012; Shin et al., 2019). In severe COVID-19, blood $CD4^+$
561 T, $CD8^+$ T and NK cells expressed markers of exhaustion (Varchetta et al., 2020), a
562 finding not mirrored in moderately sick Syrian hamsters. In contrast, T and NK
563 responses were effective and self-resolving. This matches observations of broad T cell
564 antigen-specificity in the majority of resolved cases independent of mild or severe
565 infection (Peng et al., 2020). In our study, we found SARS-CoV-2 neutralizing
566 antibodies at 5 dpi, likely of IgM type, as early appearance and corresponding elevated
567 Ighm protein levels suggested. Seroconversion in COVID-19 patients occurred 7 to 14
568 days post diagnosis with IgG titers appearing at later time points (Gudbjartsson et al.,
569 2020; Ni et al., 2020).
570 At 14 dpi, infectious virus was no longer detected in hamster lungs, and most
571 transcriptional activity had returned to basal levels. Upregulation of mitotic markers in
572 AT2 cells may reflect regeneration mechanisms after clearing the infection.
573 The pulmonary capillary microvascular niche in lungs supports alveolar epithelial repair
574 mechanisms following injury, e.g. by secretion of MMP14, VEGF, thrombospondin-1
575 (THBS1) (Mammoto and Mammoto, 2019). Analysis of pulmonary endothelial cell
576 subclusters revealed that bronchial, pulmonary capillary and pulmonary vein
577 endothelial cells showed increased expression of *Thbs1* at 5, but not 14 dpi. Similarly,
578 no increase in *Mmp14* or *Vegf* expression was detected at 14 dpi. In murine influenza
579 characterized by lung injury and pronounced alveolar damage, Niethamer et al.
580 described a pulmonary population of proliferating endothelial cells at 14 dpi (Niethamer
581 et al., 2020) that was absent in SARS-CoV-2 infected Syrian hamsters, indicating that
582 the alveolar endothelial and epithelial damage remained moderate in our model. Most
583 notably, lung endothelial cells showed an anti-fibrotic gene signature at 14 dpi (*Nr4a1*
584 (Palumbo-Zerr et al., 2015), *Akap12* (Lee et al., 2018), *Nrarp* (downstream of Notch-

signaling) (Cao et al., 2016), indicating regeneration rather than repair of lung tissue, thereby matching histopathology findings.

Our study has several limitations, including limited disease spectrum by restriction to moderate disease, lack of detailed B cell response analysis beyond 14 dpi, and need for improvement of gene annotation in the current version hamster genomes. Furthermore, it does not recapitulate the various covariates and preexisting conditions that can affect disease outcome. Clearly, we are only at the beginning of matching the course of disease in hamsters and humans in greater detail.

Nevertheless, we already provide clear evidence that Syrian hamsters recapitulate the course of moderate human SARS-CoV-2 infection. Hamsters displayed nearly prototypic antiviral immune responses starting with rapid, yet self-restricted neutrophilic response, along with a fast and strong monocytic innate immune response following activation after virus uptake, augmenting local anti-viral responses and pro-inflammatory CC chemokine production recruiting a potent type 1 T cell response that probably contributed to elimination of pulmonary residing virus via cytotoxic effector mechanisms. Neutralizing antibodies of IgM type aided in preventing viral spread and fostered cellular virus uptake. Viral infection and inflammatory response in and by lung epithelium is not predominant. Upon successful elimination of virus, alveolar epithelial repair mechanisms started, along with endothelial suppression of fibrotic programs, thus enabling pulmonary regeneration in convalesced hamsters.

Hence, Syrian hamsters represent a highly suitable model to study pathophysiology of moderate COVID-19, virus-directed and immunomodulatory therapies, and potentially vaccines. SARS-CoV-2 infected Syrian hamsters mount immune responses consistent with COVID-19 patients and enable for detailed investigations on the kinetics and role of specific cell populations, highlighting the dominant contribution of monocytic macrophages, endothelial cells and T cells to inflammatory responses and resolution of SARS-CoV-2 infection.

Data and code availability

Raw and processed data is available at the NCBI gene expression omnibus, entry GSE162208. The code used for data analysis is available at github.com, https://github.com/Berlin-Hamster-Single-Cell-Consortium. Further supplementary data is available at http://www.mdc-berlin.de/singlecell-SARSCoV2.

Author Contributions: Conceptualization, G.N., E.W., J.T and M.W.; Methodology, G.N., E.W., P.P., D.P., D.V., J.K., F.P., K.D., M.M., V.F., B.O., S.A., T.H., M.R., A.D.G., J.T.; Software/Data analysis, G.N., E.W., P.P., D.P., F.P., K.D., M.M., V.F., B.O., S-M.W., S.A., T.H., M.R., J.T.; Investigation, G.N., E.W., P.P., D.P., D.V., J.K., F.P., K.D., M.M., V.F., B.O., S-M.W., S.A., T.H., C.D., L.E.S., J.T., M.W.; resources, M.M., C.D., N.S., M.R., D.B., A.D.G., C.G., M.L., J.T., M.W.; data curation, E.W.; writing—original draft preparation, G.N., E.W., J.T. and M.W..; writing—review and editing, G.N., E.W., P.P., D.P., J.K., F.P., K.D., M.M, V.F., B.O., S-M.W., C.D., L.E.S., N.S., M.R., D.B., A.D.G, C.G., M.L., J.T., M.W.; Supervision, G.N., E.W., J.T., C.G., M.L. and M.W.; Project administration, G.N.; Funding acquisition, G.N., J.T. and M.W.. All authors have read and agreed to the published version of the manuscript."

Funding: This research was funded by a Berlin Institute of Health (BIH) grant to G.N., a German Federal Ministry of Education and Research, Germany (BMBF) grant to M.W., grant number CAPSyS (01ZX1604B), and by a German Research Foundation (DFG) grant to JT and ADG, grant number SFB-TR84 Z01b. G.N., S.-M. W. and M.W. are supported by the German Ministry of Education and Research (BMBF) and by the Agence nationale de la recherche (ANR) in the framework of MAPVAP (16GW0247). A.D.G. is supported by BMBF (NUM-COVID 19, Organo-Strat 01KX2021) and Einstein Foundation 3R (EZ-2020-597 FU). N.S. is supported by DFG, grant number SFB-TR84 B01, C09 und Z02. C.G. is supported by BMBF (NUM-COVID 19, Organo-Strat 01KX2021) and BIH. M.R. is supported by the Francis Crick Institute, which receives its core funding from Cancer Research UK (FC001134), the UK Medical Research Council (FC001134), and proteomic work in this manuscript has been conducted as part of the National Research Node 'Mass spectrometry in Systems Medicine (MSCoresys) BMBF, under grant agreement 031L0220. M.W. is supported by the German Research Foundation (SFB-TR84 C06 and C09, SFB1449 B02), by the German Ministry of Education and Research (BMBF) in the framework of CAPSyS-COVID (01ZX1604B), PROVID (01KI20160A), SYMPATH (01ZX1906A), NUM-NAPKON (01KX2021) and by the Berlin Institute of Health (CM-COVID).

Acknowledgments: The authors sincerely thank Drs. Jasmin Lienau and Alexis Vogelzang for excellent manuscript and figure editing. Computation has been performed on the HPC for Research cluster of the Berlin Institute of Health. The

authors thank Angela Linke, Michaela Scholz and Simon Dökel for excellent technical assistance with histopathology and ISH.

Conflicts of Interest: G.N. received funding for research from Biotest AG. E.W. P.P, D.P.,D.V.,J.K., F.P., K.D., M.M., V.F., B.O., S.-M.W, S.A., T.H., B.S., C.D., L.E.S., N.S., M.R., D.B., A.D.G., C.G., M.L., J.T declare no conflict of interest.
M.W. received funding for research from Actelion, Bayer Health Care, Biotest AG, Boehringer Ingelheim, Noxxon, Pantherna, Quark Pharma, Vaxxilon, and for advisory from Actelion, Aptarion, Astra Zeneca, Bayer Health Care, Berlin Chemie, Biotest, Boehringer Ingelheim, Chiesi, Glaxo Smith Kline, Novartis, Noxxon, Pantherna, Teva and Vaxxilon.

The funders had no role in the design of the study, in the collection, analyses, or interpretation of data, in the writing of the manuscript, or in the decision to publish the results.

Figure legends:

Figure 1: Single-cell dynamics in lungs and blood of SARS-CoV-2 infected Syrian hamsters

(a), UMAP plot of identified cell populations in Syrian hamster lungs. (b), Cell count of isolated cells per lung lobe over time (2, 3, 5 and 14 dpi) and control group (naïve, “d0”). (c), Count of hematopoietic cells per lung lobe in naïve hamsters and over time pi. (d), Changes in cellular density of lung cells in UMAP projection. Coloration indicates log2 fold change between control group and 5 dpi. (e), Percentage of hematopoietic cells per lung lobe in naïve hamsters and over time pi. (f), UMAP plot of identified cell populations in blood samples. (g), Cell count of isolated cells per mL blood in naïve hamsters and over time pi. (h), Percentage of identified cell populations in blood samples over time pi and naïve animals. (i), Neutrophil–lymphocyte ratio in blood samples over time pi and naïve animals. (a, d and f), Clusters defined by Louvain clustering, n = 3 per time point. (b, c, e, g, h and i), Data display means ± SD. n = 3 per time point. Ordinary one-way ANOVA, Sidak’s multiple comparisons test versus corresponding 0 dpi (naïve). $*$ $P < 0.05$, $**$ $P < 0.01$, $***$ $P < 0.001$, $****$ $P < 0.0001$

Figure 2: Proteomics analysis recapitulates transcriptomics and human COVID-19 patient data

(a), Temporal evolution of gene ontology/biological process terms connected with immune system response in lung tissue (left part) and in serum fluid (right part), for the indicated time points compared to samples from uninfected animals. Enriched terms were filtered for terms mentioning “immune”, “interferon”, “neutrophil”, “T cell” and “B cell”. Size of dots correspond to the inverse of the false discovery rate. (b), Expression values for differentially regulated proteins in hamster serum (control 3 dpi, p value < 0.01) and lung (control 5 dpi, p value < 0.01) that correlate with disease severity in human plasma. Controls from different days are plotted together. The thick line represents median of all values, lower and upper hinges correspond to medians of lower and upper half of set, respectively. Whiskers extend to a maximum of 1.5 times distance between first and third quartile. All values are shown. (c) Expression values for the differentially expressed proteins Lgals3 and Lgals3bp (only detected in lung samples).

Figure 3: Induction of inflammatory mediators are strongest and earliest in myeloid cells

Dotplots of differentially expressed cytokines and inflammatory mediators in lungs. Shown are genes that display a significant absolute log2-transformed fold change of at least one in at least one comparison, and are grouped into four categories indicated on the left. Coloration and point size indicate log2-transformed fold changes and *P* values, respectively, of genes at 2 dpi relative to control groups (naïve). Adjusted *P* values were calculated by DEseq2 using Benjamini-Hochberg corrections of Wald test *p* values. Genes are ordered by unsupervised clustering, cell type as in Figure 1.

Figure 4: Transcriptional response to SARS-CoV-2 infection is strong in myeloid and moderate in epithelial cells

(a, b), Dotplot of differentially expressed genes in lungs (a) and blood (b). Shown are genes that are in at least one cell type among the top 4 most changing genes as ranked by adjusted *p* value. Example: top 4 most changing genes in alveolar macrophages are *Ybx3*, *Rps15*, *Rps10*, and *Uba52*. Coloration and point size indicate log2-transformed fold changes and *p* values, respectively, of genes at 2 dpi relative to control groups (naïve). Adjusted *p* values were calculated by DEseq2 using Benjamini-

Hochberg corrections of Wald test *p* values. Cell types and genes are ordered by unsupervised clustering. (c), Top, fraction of monocytic macrophages expressing *Cxcl10* in blood and lungs from naïve animals and 2 dpi. Bottom, boxplots of *Cxcl10* gene expression values of cells positive for *Cxcl10* expression. Significance levels were calculated using generalized linear mixed-effects models for bar plot and a Wilcoxon rank sum test on all cells (i.e. not only the ones expressing the gene) for boxplots. * means *p* value 0.05-0.01, ** means *p* value 0.01-0.0001, *** means *p* value smaller 0.0001. See materials and methods for details. (d), As in (c), but only in lungs, all time points and both alveolar epithelial cells type 2 (AT2) and monocytic macrophages. Displayed are values for *Isg15* (left) and *Cxcl10* (right). For all bar plots, data display means ± SD, n = 3 per time point. For all boxplots, lower and upper hinges correspond to first and third quartiles. Whiskers extend to a maximum of 1.5 times the distance between first and third quartile. Outliers beyond are marked by single dots.

Figure 5: Virus RNA in monocytic macrophages leads to dose-dependent activation of pro-inflammatory cytokines by TLR signaling

(a), Feature plots of entry factor expression in UMAP projection. Coloration indicates expression values of indicated genes. (b-e), Detection of viral RNA by in situ-hybridization. Labeled are supposed endothelium (b, hash), bronchial epithelial cells (b, arrowhead), AT1 (c, arrowhead) and AT2 (c, arrow). (d, inset), macrophages containing viral RNA and cell debris (arrowhead), and an example of high levels of viral RNA without cell debris in the inset (arrow). For (b-e), red signals viral RNA and blue hemalaun counterstain. Time points: (b-c) from 2 dpi, (d) from 3 dpi, (e) from naïve. Bars: (b, d, e) = 50 µm, (c) = 100 µm, Inset in (c) = 20 µm. (f), Cells in the UMAP projection are colored by amount of viral RNA (log10 transformed percentage of viral RNA per cell), along with overview of identified cell types in lungs. (g), Dotplot of cytokine expression in monocytic macrophages containing viral RNA compared to those without viral RNA. Coloration and point size indicate log2 fold change and *P* value for each time point 2, 3 and 5 dpi. (h, i), Box- and barplots of *Isg15* (h) and *Cxcl10* (i) gene expression in AT2 and monocytic macrophages along, comparing cells containing viral RNA to those without for 2, 3, and 5 dpi. Barplot shows percentage of cells positive for respective gene, with mean ±SD, n = 3. Boxplots show gene expression levels in cells positive for respective gene. (j), Box- and barplots of *Cxcl10* in monocytic macrophages and fraction of *Cxcl10* positive cells for each time point pi

and naïve animals, with cells grouped by increasing virus levels for 2, 3, and 5 dpi. (e and f), for barplots, data display means ± SD. Significance levels calculated using generalized linear mixed-effects models for barplot and a wilcoxon rank sum test on all cells (i.e. not only the ones expressing the gene) for boxplots. * means *p* value 0.05-0.01, ** means *p* value 0.01-0.0001, *** means *p* value smaller 0.0001. See materials and methods for details.

Figure 6: Endothelial cells show subtype and time specific activation of cytokines

(a), UMAP plot of lung endothelial cell subpopulations. (b), Dotplot of differentially expressed genes in lung endothelial cell subpopulations over time. Shown are genes that are in at least one cell type among the top 10 most changing genes as ranked by adjusted *p* value. (c), Dotplot of differentially expressed genes from two curated sets as indicated in lung endothelial cell subpopulations over time pi. For both (b) and (c), coloration and point size indicate log2-transformed fold changes and *P* values, respectively, of genes at 2 dpi relative to control groups (naïve). Adjusted *P* values were calculated by DEseq2 using Benjamini-Hochberg corrections of Wald test *P* values.

Figure 7: Syrian hamsters exhibit a strong cytotoxic T/NK cell response at day 5 post infection

(a), UMAP plot of lung T/NK cell subclustering indicating cell subpopulations. (b), Count of lung T cell subpopulations and NK cells per lung lobe. (c), Dotplot of master regulators of T cell differentiation and effector genes. Coloration and point size indicate log2 fold change and *P* value, respectively. (d), Fraction of *Ifng*$^+$ cells in CD4$^+$ T, CD8$^+$ T and NK cells at 2, 3, 5 and 14 dpi and naïve. (e), Fraction of *Gzma*$^+$ cells in CD8$^+$ T cells at 2, 3, 5 and 14 dpi and naïve. (f), Fraction of AT2 cells, monocytic macrophages, endothelial cells and AT1 cells containing both at least one cell type marker gene (AT2: *Sftpa1*, *Sftpc* – monocytic macrophages: *Fcn1*, *Saa3* – endothelial cells: *Cldn5*, *Plvap* – AT1: *Ager*, *Aqp5*) together with *Gzma*. Data display means ± SD, n = 3 per time point. (g), Histopathology of blood vessels at different time points, bar: 50 µm. (h) Serum neutralization titers of SARS-CoV-2 infected hamsters at 5 and 14 dpi. Serum titers of naïve, 2 and 3 dpi did not neutralize up to detection limit 1:4 (dotted line). Data display n = 3 with mean per time point.

Methods

Ethics statement, animal husbandry and study design

All experiments involving animals were approved by institutional and governmental authorities (Freie Universität Berlin and Landesamt für Gesundheit und Soziales Berlin, Germany, approval number 0086/20) and performed in accordance with relevant national and international regulations. Female and male Syrian hamsters (*Mesocricetus auratus*; breed RjHan:AURA, Janvier Labs, Saint-Berthevin, France) were housed in biosafety level 3 (BSL-3) conditions in individually ventilated cages with enrichment (IVCs; Tecniplast, Buguggiate, Italy; Carfil, Oud-Tunrhout, Belgium). Food and water was provided *ad libidum*. Daily cage temperature and relative humidity measurements ranged from 22–24 °C and 40–55 %, respectively. Animals were acclimatized for a minimum of 7 days prior to infection.

Virus Stocks

SARS-CoV-2 isolate (BetaCoV/Germany/BavPat1/2020) [32235945] was kindly provided by Daniela Niemeyer and Christian Drosten, Charité Berlin, Germany. Virus stocks were propagated under BSL-3 conditions in Vero E6 cells (ATCC CRL-1586) in minimal essential medium (MEM; PAN Biotech, Aidenbach, Germany) supplemented with 10 % fetal bovine serum (PAN Biotech), 100 IU/mL penicillin G and 100 g/mL streptomycin (Carl Roth, Karlsruhe, Germany). All hamsters described here received virus from the same batch.

Animal infection

At 10–12 weeks of age hamsters were intranasally infected with 1 x 10^5 pfu SARS-CoV-2 under anesthesia as previously described (Osterrieder et al., 2020). Clinical signs and weight were monitored daily. Animals with >15 % body weight loss over 48 h were euthanized in accordance with the animal use protocol. Naïve (n = 3) and infected hamsters were randomly selected for analyses at time points 2, 3, 5 or 14 days post infection (dpi) (n = 3, each). Exsanguination and euthanasia under anesthesia were performed as previously described (Osterrieder et al., 2020). 1 mL peripheral blood was collected in EDTA-coated syringes. The left lung lobe was collected for histopathology, the right caudal lobe for single-cell analysis, the right cranial lobe for virological assessments and the right medial for bulk RNA as well as

proteomics analysis. Experimental design and analysis are summarized in the supplemental material (Figure S1).

Viral burden assessment in lungs and tracheal swabs

Virus titers were determined by serial dilutions of lung homogenates (50 mg) plated on Vero E6 cells. Virus adsorption was allowed for 2 h, medium was then removed and cells were overlaid with MEM supplemented with 5 % FBS, 100 IU/mL penicillin G and 100 g/mL streptomycin and 1.25 % Avicel (Sigma-Aldrich, St. Louis, MO) and incubated for 48 h. Cells fixed in 4 % formalin were stained with 0.75 % crystal violet in aqueous solution and plaques were counted.

For *RNA extractions and quantitative RT-PCR,* RNA from oropharyngeal swabs, 25 mg lung tissue and 25 µL whole blood was isolated with the innuPREP Virus DNA/RNA Kit (Analytic Jena) according to the manufacturer's instructions. One-step RT qPCR reaction with the NEB Luna Universal Probe One-Step RT-qPCR (New England Biolabs) and the 2019-nCoV RT-qPCR primers and probe (E_Sarbeco) [31992387] quantified viral RNA according to the manufacturer's instructions and normalization of viral RNA to cellular *Rpl18* occurred as previously described [32698441]. Primers and probes are listed in the Supplemental Material (Table S1), standard curves for quantification were generated as previously described [32698441]. Viral RNA copies were calculated per 1x10^5 hamster *Rpl18* transcripts.

Measurement of neutralizing antibodies titer

Serum neutralization tests were performed by two fold serial dilutions (1:4 to 1:512) of complement inactivated (56°C, 2 h) hamster serum plated on sub-confluent monolayers of Vero E6 cells in 96 well plates. 50 pfu SARS-CoV-2 were added per well and incubated for 72 h at 37°C, fixed with 10 % formalin for 24 h and stained with crystal violet (0.75% aqueous solution). Serum neutralization was considered effective in wells that did not shows any cytopathic effect, the highest effective dilution was counted.

Histopathology and *in situ*-hybridization of SARS-CoV-2 RNA

For histopathology and *in situ*-hybridization (ISH), lungs were processed as described (29361238). Left lung lobes were immersion-fixed in 10 % formalin, pH 7.0, for 48 h, embedded in paraffin, and cut into 2 µm sections. Hematoxylin and eosin (HE) staining

and *in situ*-hybridizations were performed as described [32817952] using the ViewRNA™ ISH Tissue Assay Kit (Invitrogen by Thermo Fisher Scientific, Darmstadt, Germany) following the manufacturer's instructions with minor adjustments. SARS-CoV-2 RNA was localized with probes detecting N gene sequences (NCBI database NC_045512.2, nucleotides 28,274 to 9533, assay ID: VPNKRHM). An irrelevant probe for the detection of streptococcal pneumolysin was used to control for sequence-specific binding (Bertzbach et al., 2020). Amplifier and label probe hybridizations were performed following the manufacturer's instructions using fast red as chromogen with hemalaun counterstain. Tissues were histopathologically evaluated by board-certified veterinary pathologists (KD, ADG) in a blinded fashion following standardized recommendations (Gruber et al., 2020), including pneumonia-specific scoring parameters (Dietert et al., 2017) as previously described for SARS-CoV-2 infection in hamsters (Osterrieder et al., 2020).

Single Cell Isolation from Whole Blood

Protocols were adapted for BSL-3 facility regulations. For isolation of cells from whole blood, 250 µL blood were lysed in red blood cell lysis buffer (BioLegend), washed and centrifuged according to the manufacturer's instructions. Resulting RBC-free pellets were resuspended in low-BSA buffer (1× PBS, 0.04 % BSA), filtered with 40 µm FloMi filters (Merck) suitable for volumes below 500 µL and counted microscopically by hemocytometer in trypan blue.

Single Cell Isolation from Hamster Lungs

Protocols were adapted for BSL-3 facility regulations. For isolation of single cells *lobus caudalis* of the right lung was removed and placed in storage medium (1× PBS, 0.5 % BSA) until further processing. Storage and isolation media contained 2 µg/mL ActinomycinD. Tissues and cells were centrifuged at 350 x *g* for 6 minutes at 4 °C. Lung lobes were mechanically disassociated with tweezers for 2 minutes in enzymatic digestion mediumcontaining 3.4 mg/mL Collagenase Cls II (Merck) and 1 mg/mL DNase I (PanReac AppliChem) in 2 mL Dispase medium (Corning) per lung lobe followed by 30 minutes incubation at 37 °C and 5 % CO_2. After repeated pipetting of digested lung tissue with 5 mL pipettes, cell suspensions were pressed through 70 µm cell strainers with syringe plungers. Red blood cells were lysed (BioLegend), washed with an excess of PBS/BSA and resuspended in low-BSA buffer (1× PBS, 0.04 %

BSA), and filtered with 40 µm low-volume FloMi filters (Merck). Cells were counted with trypan blue.

Single Cell RNA Sequencing

Barcoding, cDNA Library generation and *sequencing*; Filtered cells were adjusted to a final concentration of ~1,000 cells / µL in 1× PBS with 0.04% BSA and subjected to partitioning into Gel-Beads-in-Emulsions (GEMs) with the aim of recovering a maximum of 6,000 single cells per hamster and organ by following the instructions for the Chromium Next GEM Single Cell 3′ GEM, Library & Gel Bead Kit v3.1 provided by the manufacturer (10x Genomics). The procedure entailed tagging polyadenylated mRNA from individual cells with unique 16-bp 10x barcodes and 10-bp Unique Molecular Identifiers (UMI). Following instructions, reverse transcribed full-length and barcoded cDNA were bulk-amplified. Enzymatic fragmentation and size selection followed, resulting in double-stranded cDNA amplicons optimized for library construction. Adaptor ligation and sample index PCR introduce all reads, sequences and sample index into the cDNA library necessary for Illumina bridge amplification and sequencing.

Single-cell libraries were quantified using Qubit (ThermoFisher) and quality-controlled using the Bioanalyzer system (Agilent). Sequencing was performed on a Novaseq 6000 device (Illumina), with SP or S1 flow cells (read1: 28 nucleotides, read2: 64 nucleotides).

Bulk RNA sequencing

For *lung RNA Bulk Sequencing,* the *lobus medialis* of the right lung lobe was removed carefully and stored in RNA Later Solution for a maximum of 24 hours at 4 °C (Thermofisher). Lung Tissue was homogenized using the TissueLyser II system (Qiagen) and the homogenate stored in Trizol reagent (Zymo research). For *WBC RNA Bulk Sequencing*, white blood cells were isolated as described for scSeq followed by lysis in Trizol reagent. RNA extractions were performed according to the Direct-zol RNA Miniprep protocol (Zymoresearch). Bulk RNA sequencing libraries constructed using the Nebnext Ultra II Directional RNA Library Prep Kit (New England Biolabs), and sequenced on a Nextseq 500 device with read length 76.

Proteomics

Sample preprocessing

Approximately 5 mg homogenized lung tissue and 5 µl of hamster serum were added to the lysis and inactivation buffer (RIPA) and boiled for 10 min at 95 °C before storage at -80 °C. Samples were thawed on ice and 20 µl of the extract were transferred to a 96 well plate. The volume was adjusted to 50 µl with water and 25 µl of 50 U benzonase, 50 mM ABC, 2 mM $MgCl_2$ added before incubation for 30 min at 37 °C. The lysates were processed on a Biomek i7 workstation using the SP3 protocol as previously described with single-step reduction and alkylation (Muller et al., 2020). In brief, 20 µl reduction and alkylation buffer (40 mM TCEP, 160 mM CAA, 200mM ABC) were added and the samples were incubated for 5 min at 95 °C. To bind the proteins, 200 µg paramagnetic beads (1:1 ratio of hydrophilic/hydrophobic beads) were added and proteins precipitated with 50 % ACN. The samples were washed 3 times with EtOH and once with ACN, before reconstitution in 35 µl 100 mM ABC, addition of 20 µl trypsin (1 µg) ON digestion at 37 °C. The reaction was stopped by addition of formic acid to a final concentration of 0.1 %. Samples were then transferred to a new plate and used for LC-MS/MS analysis without additional conditioning or clean-up.

For proteomics, we combine conventional approaches with latest generation acquisition methods, (i.e. Scanning SWATH) (Messner et al., 2020a) coupled with high flow chromatographic separation. This combination combines the strengths of the depth of conventional proteomics, with the strength of very high measurement precision at high throughput achieved with the high-flowrate LC proteomic methods, which overcome limits in the clinical application of proteomics.

Liquid Chromatography−Mass Spectrometry Analysis (LC−MS)

High-throughput analysis of serum and lung tissue; Peptide separation has been accomplished in a 5-minute water to acetonitrile gradient on an Agilent Infinity II HPLC coupled to a Sciex Triple TOF 6600 mass spectrometer (IonDrive TurboV Source) operating in ScanningSWATH mode with minor changes in the liquid chromatography method (Messner et al., 2020a). As follows: 5 µg of peptides were loaded and resolved in a linear gradient from 1-35 % buffer B in 4.5 min before increasing to 40 % B in 0.5 min and washing for 0.2 min with 80 % buffer B before equilibration for 2.2 min with initial conditions (buffer A: 0.1 % formic acid, buffer B: 100 % ACN, 0.1 % formic acid).

Computational proteomics; For *Mesocricetus auratus* serum samples, a project specific library was generated by gas-phase fractionation (GPF), whereas the lung

tissue library was constructed using standard settings in library free mode with DIA-NN (version 1.7.12) (Demichev et al., 2020a). Proteins were annotated using the *M. auratus* genome sequence generated in this work. The libraries were automatically refined based on the project dataset at 0.01 global q-value (using the "Generate spectral library" option in DIA-NN) as previously described (Messner et al., 2020b). The output was filtered at 0.01 false discovery rate (FDR) at the peptide level. For GPF, 6 single 1 µg injections of pooled serum samples were analyzed by online nanoflow liquid chromatography tandem mass spectrometry on a Ultimate3000 Thermo Scientific Q Exactive Orbitrap, LC-MS instrument (Thermo Fisher Scientific, Waltham, USA). The peptides were concentrated for 3 min on a trap column (PepMap C18, 5 mm x 300 µm x 5 µm, 100Å, Thermo Fisher Scientific) with a buffer containing 2:98 (v/v) acetonitrile/water containing 0.1% (v/v) trifluoroacetic acid at a flow rate of 20 µl/min. They were separated by a 250 mm LC column (Acclaim PepMap C18, 2 µm; 100 Å; 75µm, Thermo Fisher Scientific). The mobile phase (A) was 0.1 % (v/v) formic acid in water, and (B) 80 % acetonitrile in 0.1 % (v/v) formic acid. In 155 min total acquisition time gradient B increased in 90 min to 25 %, and in 30 min to 40 % with a flow rate of 300 nl/ min. The MS instrument was operated in the data independent mode as followed: the Orbitrap worked in centroid mode with 4 m/z DIA spectra (4 m/z precursor isolation windows at 17,500 resolution, AGC target 1e6, maximum inject time 60 ms, 27 NCE). An overlapping window pattern from narrow mass ranges using window placements (i.e., 395-505, 495-605,595-705, 695-805,795-805,895-905 m/z) was set. Two precursor spectra, a wide spectrum (395-505 m/z at 35,000 resolution) and a narrow spectrum matching the range using an AGC target of 1e6 and a maximum inject time of 60 ms were interspersed every 25 MS/MS spectra at resolution of 17,500. Typical mass spectrometric conditions were as follows: spray voltage, 2.1 kV; no sheath and auxiliary gas flow; heated capillary temperature: 275 °C; normalized HCD collision energy 27 %. As lock mass acted the background ion m/z 445.1200.

Materials Proteomics; Hydrophobic Sera-Mag magnetic carboxylate modified particles (44152105050250 Fisher Scientific), hydrophilic Sera-Mag magnetic carboxylate modified particles (24152105050250 Fisher Scientific), Twintec skirted low bind plates (0030129512 Eppendorf), TCEP (646547 Sigma Aldrich), SDS (A7249.1000 Applichem), CAA (22788 Merck/Millipore), ammonium bicarbonat (/871.2 Roth), 100 % ACN (955-212 Fisher Scientific), 80 % ethanol (1.00983.2500 Millipore), 230 µl Biomek Tips (B85903 Beckmann Coulter), Eppendorf 500 µl deep well plates

(30501101 Eppendorf), Waters Acquity UPLC 700 µl plates (186005837 Waters GmbH) Sequencing grade modified Trypsin (V5117 Promega), Pierce Quantitative Fluorometric Peptide Assay (number 23290), formic acid (85178 Thermo Scientific), water (1.15333.2500 Merck), protease inhibitor cocktail complete mini (Roche 04693124001), benzonase nuclease (Sigma Aldrich E1014-25KU)

Data pre-processing; Four serum samples showed low quality and were removed. Peptides with excessive missing values (> 30% per group) were excluded from analysis. Batch correction was applied. The peptide matrix was filtered using factor "Proteotypic" keeping only peptides belonging to one protein group. To obtain a quantitative protein data matrix, the log2-intensities of peptides belonging to one protein group were summarised by "maxLFQ" method (Cox et al., 2014) into protein log intensity.

Statistical analysis; Statistical analysis of proteomics data was carried out using internally developed R scripts. Linear modelling was based on the R package LIMMA (Ritchie et al., 2015). Following model was applied to the sets of lung/serum samples (log(p) is log2 transformed expression of a protein): log(p) ~ 0 + Class(Day) + Gender

Here, categorical factor Class(Day) has 8 levels:

Infected(D02), Infected(D03), Infected(D05), Infected(D14),

Control(D02), Control(D03), Control(D05), Control(D14)

Categorical factor Gender has two levels: male, female.

The following contrasts were evaluated to trace time dependence of response to viral infection (Note that Contrast5 addresses the average difference between infected and recovered animals and Contrast6 addresses the difference between infected and control animals on average):

Contrast1: Infected(D02) – Control(D02)

Contrast2: Infected(D03) – Control(D03)

Contrast3: Infected(D05) – Control(D05)

Contrast4: Infected(D14) – Control(D14)

Contrast5: [Infected(D02)+Infected(D03)+Infected(D05)]/ 3 [Control(D02)+ Control(D03)+ Control(D05)]/3 – [Infected(D14) – Control(D14)]

Contrast6: [Infected(D02)+Infected(D03)+Infected(D05)]/3 – [Control(D02)+ Control(D03)+ Control(D05)]/3

In serum set of samples there was only one control group at 3 dpi and it was used to build contrasts replacing control groups at other dpi's.

For finding regulated features following criteria were applied:
Significance level alpha was set to guarantee false discovery rate below 10% at the response maximum (5 dpi) in both sample types. We found that alpha = 0.01 was delivering regulated proteins with Benjamini–Hochberg FDR below 8% in lung tissue and below 6% in serum and used it for feature selection.
The log fold change criterion was applied to guarantee that the measured signal is above the average noise level. As such we have taken mean residual standard deviation of linear model: log2(T) = mean residual SD of linear modelling (T = 1.45 in lung and T=1.37 in serum).
Functional analysis of proteomics data; Functional analysis was carried out using gprofiler2 R package (Kolberg and Raudvere, 2020). For selecting the most (de)regulated GO terms we applied filter: 2 ≤ term size ≤ 200. Analyses for each Contrast 1 – 6 (Table 1) and then all in parallel were carried out with Benjamini–Hochberg FDR threshold 0.2. Organism for search was specified as mauratus – Mesocricetus auratus (Syrian hamster). Statistical domain scope was set to custom, list of all identified proteins was provided as background.

Statistical Analyses of clinical data

Graph-Pad Prism v8 (GraphPad Software Inc., San Diego, CA, USA) software was used for statistical analysis of clinical data. The statistical details of all analyzed experiments are given in the respective figure legends.

Annotation of the *M. auratus* genome

The *M. auratus* genome (MesAur1.0) sequence and annotation (gtf file, version 99) was downloaded from Ensembl. We noticed that 3'-UTRs in this annotation were frequently too short to capture all transcriptome reads and particularly the 3' end reads in single-cell RNA-sequencing, so we extended all 3'-UTRs for coding genes by 1,000 bp. The *Ifit2* gene was extended by 2,000 bp. For key genes analyzed in this manuscript, we verified that this extension did not lead to overlaps with downstream genes.
The Ensemble annotation was extended by mapping ENSEMBL gene ids without annotated gene names to entrez identifiers and to the homolog associated gene names using biomaRt (Durinck et al., 2009). Wherever existing, we extracted the gene name from the NCBI's All_Mammalia.gene_info (download from

ftp://ftp.ncbi.nlm.nih.gov/gene/DATA/GENE_INFO/Mammalia/) table, capturing 1067 gene names. Otherwise we used available homolog associated gene names yielding 1193 additional entries.

Analysis of bulk RNA-sequencing data

Reads were aligned to the genome using hisat2 (Kim et al., 2019) and quantified using quasR (Gaidatzis et al., 2015). We then performed gene set enrichment analysis with tmod (Zyla et al., 2019) and Hallmark, Reactome and GO BP gene sets from MSigDB v7.0 (Liberzon et al., 2015), ranking genes by the product of the sign of the log2 fold change and log10 adjusted p-value and converting hamster gene names to human using the biomaRt mouse-to-human mapping.

Analysis of single-cell RNA-sequencing data

Data analysis was done in R (R Core Team, 2019), using Seurat (Butler et al., 2018) and packages from tidyverse (Wickham et al., 2019) and glmer (Bates et al., 2015). All used code with annotation is available through Github at https://github.com/Berlin-Hamster-Single-Cell-Consortium.

Raw single-cell sequencing data was processed using CellRanger 3.1.0 (10x Genomics) with standard parameters, based on a combined MesAur1.0/SARS-CoV-2 (GenBank entry MN908947) reference. Raw feature barcode matrices from the CellRanger output were read into Seurat using the Read10X function and a Seurat object created using the CreateSeuratObject function. Cells with more than 7 % mitochondrial reads, based on the percentage feature expression of the mitochondrial genes *Cox1*, *Cytb*, *Nd1*, *Nd2*, *Nd4*, *Nd5*, *Nd6* were excluded (reads from other mitochondrial genes were not detected in the data). Furthermore, cells with less than 1000 (lung) or 500 (blood) detected genes were also excluded from downstream analysis. Sample sets (all lung, or all blood, or blood/lung combined from the individual time points) were then integrated using the SCTransform workflow, as illustrated on the Seurat website (Stuart et al., 2019). Briefly, the Seurat object was split by the hamster that the data points originated from and separately transformed using SCTransform to normalise and scale the data. To prevent batch specific/animal specific effects from obscuring results, these split objects were integrated using the SelectIntegrationFeatures, PrepSCTIntegration, FindIntegrationAnchors and IntegrateData functions in succession. PCA and UMAP dimensional reduction

analyses respectively were performed on the integrated object, using 30 dimensions for the UMAP as the SCT workflow reportedly shows more robust results with higher dimensionality. Cells were subjected to Louvain clustering using the FindNeighbours and FindClusters (with a resolution parameter of 0.8 for lung samples and 0.5 for the blood samples) functions.

To annotate cell types in the lung scRNAseq data, we used Seurat's TransferData workflow (Stuart et al., 2019) and two different reference data sets: Tabula Muris (Tabula Muris Consortium, 2018) and the Human Lung Cell Atlas (Travaglini et al., 2020). Integration with mouse data was performed using matching gene names between mouse and hamster, while gene names in the human data were converted to mouse using biomaRt. We then used the predicted cell type of the majority of cells in each cluster to guide cluster annotation, also taking into account cell marker genes published in literature and cell marker databases (Franzen et al., 2019; Zhang et al., 2019). The following populations were confirmed: Alveolar macrophages (*Siglecf*$^{+}$, *Marco*$^{+}$) (Han et al., 2018), interstitial macrophages (*C1qb*$^{+}$) (Angelidis et al., 2019), monocytic macrophages (*Ccr2*$^{+}$, *Ccr5*$^{+}$, *Arg1*$^{+}$) (Lechner et al., 2017; Shaheen et al., 2019), *Treml4*$^{+}$-monocytes (*Treml4*$^{+}$) (Briseno et al., 2016), neutrophils (*S100a8*$^{+}$, *Cxcr2*$^{+}$, *Camp*$^{+}$) (Schulte-Schrepping et al., 2020; Zhao et al., 2019), myeloid dendritic cells (mDC) (*Flt3*$^{+}$, *H2-Ab1*^{hi}, *Irf8*^{lo}, *Tcf4*^{lo}) and plasmacytoid dendritic cells (pDC) (*Flt3*$^{+}$, *H2-Ab1*^{hi}, *Irf8*^{hi}, *Tcf4*^{hi}) (Dutertre et al., 2019; Monaghan et al., 2019; Rodrigues et al., 2018; Tabula Muris Consortium, 2018), T / NK / cells (*Cd3e*$^{+}$, *Cd4*$^{+}$ or *Cd8a*$^{+}$, *Gzma*$^{+}$, *Nkg7*$^{+}$) (Raredon et al., 2019; Smith et al., 2020; Tabula Muris Consortium, 2018; Zhao et al., 2019; Zhu et al., 2009), B cells (*Cd79b*$^{+}$, *Ms4a1*$^{+}$) (Cohen et al., 2018; Schulte-Schrepping et al., 2020), alveolar epithelial cells type 1 (*Rtkn2*$^{+}$) (Angelidis et al., 2019), endothelial cells (*Pecam1*$^{+}$) (Han et al., 2018), ciliated epithelial cells (*Foxj1*$^{+}$) [30318149], alveolar epithelial cells type 2 (*Lamp3*$^{+}$) (Cohen et al., 2018), smooth muscle cells (*Tagln*$^{+}$, *Acta2*$^{+}$) (Angelidis et al., 2019; Tawfik et al., 2014), fibroblasts (*Dcn*$^{+}$) (Angelidis et al., 2019) as well as myofibroblasts (*Dcn*$^{+}$, *Tagln*^{hi}, *Acta2*^{hi}).

Analysis of single-cell sequencing data for blood samples was similar to that of lung samples with minor exceptions. Following initial clustering, cluster marker genes were identified using the FindAllMarkers function and clusters expressing high levels of erythrocyte marker genes *Snca*, *Fam46c* and *Alas2* were identified as containing erythrocyte contamination (Barbour et al., 2008; Chiabrando et al., 2014; Durussel et al., 2016). Cells in these clusters, as well as a cluster of most likely dead cells, marked

by the expression of mitochondrial genes, were removed and the data was re-integrated using the workflow described above. Cell type annotations were assigned to the identified cluster using the follow marker genes: Classical (inflammatory) monocytes (*Ccr2*$^{+}$, *Cx3cr1*^{lo}, *Adgre1*$^{+}$); non-classical (residential) monocytes (*Ccr2*$^{-}$, *Cx3cr1*^{hi}, *Adgre1*$^{+}$) (Burgess et al., 2019; Cochain et al., 2018; Ronning et al., 2019); mature neutrophils (*Cxcr2*$^{+}$, *S100a8*$^{+}$, *Camp*^{lo}, *Retn*^{lo}, *Ltf*^{lo}) and immature neutrophils (*Cxcr2*$^{+}$, *S100a8*$^{+}$, *Camp*^{hi}, *Retn*^{hi}, *Ltf*^{hi}) (Kim et al., 2017; Schulte-Schrepping et al., 2020; Xie et al., 2020; Zhao et al., 2019); myeloid dendritic cells (*Flt3*$^{+}$, *H2-Ab1*^{hi}, *Irf8*^{lo}, *Tcf4*^{lo}) and plasmacytoid dendritic cells (*Flt3*$^{+}$, *H2-Ab1*^{hi}, *Irf8*^{hi}, *Tcf4*^{hi}) (Dutertre et al., 2019; Monaghan et al., 2019; Rodrigues et al., 2018; Tabula Muris Consortium, 2018); T cells (*Cd3e*$^{+}$, *Cd4*$^{+}$ or *Cd8a*$^{+}$) and activated T cells (*Cd3e*$^{+}$, *Cd4*$^{+}$ and/or *Cd8a*$^{+}$, *Gzma*$^{+}$) (Raredon et al., 2019; Tabula Muris Consortium, 2018; Zhao et al., 2019; Zhu et al., 2009), natural killer (NK) cells (*Cd3e*$^{-}$, *Nkg7*$^{+}$) (Smith et al., 2020; Zhao et al., 2019); B cells (*Cd79a*$^{+}$, *Ms4a1*$^{+}$) (Cohen et al., 2018; Schulte-Schrepping et al., 2020; Zuccolo et al., 2013) and platelets (*Gng11*$^{+}$, *Ppbp*$^{+}$) (El-Gedaily et al., 2004; Schoggins, 2019). While cluster 17 showed no expression of *Ccr2*, the levels of *Adgre1* and *Cd14* were considerable and it was considered as comprising classical monocytes for the purposes of this study (Sampath et al., 2018).

Previously published scRNAseq data of bronchoalveolar lavages originating from COVID-19 patients data from Liao et al. (Liao et al., 2020) was processed using the same (Seurat) workflow in R. We kept cells with less than 10 % mitochondrial reads, less than 50000 UMIs and less than 6000 genes and used IntegrateData to combine different samples. We then again used the Human Lung Cell Atlas reference and TransferData to annotate clusters.

Differential cell density was calculated as in (Praktiknjo et al., 2020) by plotting the log2 ratio of two separate 2D kernel density estimators interpolated on the UMAP coordinates of each cell.

References

10x Genomics (2020). Can I process neutrophils (or other granulocytes) using 10x Single Cell applications?

1159 Ackermann, M., Verleden, S.E., Kuehnel, M., Haverich, A., Welte, T., Laenger, F.,
1160 Vanstapel, A., Werlein, C., Stark, H., Tzankov, A.*, et al.* (2020). Pulmonary Vascular
1161 Endothelialitis, Thrombosis, and Angiogenesis in Covid-19. N Engl J Med *383*, 120-
1162 128.
1163 Angelidis, I., Simon, L.M., Fernandez, I.E., Strunz, M., Mayr, C.H., Greiffo, F.R.,
1164 Tsitsiridis, G., Ansari, M., Graf, E., Strom, T.M.*, et al.* (2019). An atlas of the aging
1165 lung mapped by single cell transcriptomics and deep tissue proteomics. Nat Commun
1166 *10*, 963.
1167 Barbour, R., Kling, K., Anderson, J.P., Banducci, K., Cole, T., Diep, L., Fox, M.,
1168 Goldstein, J.M., Soriano, F., Seubert, P.*, et al.* (2008). Red blood cells are the major
1169 source of alpha-synuclein in blood. Neurodegener Dis *5*, 55-59.
1170 Bates, D., Mächler, M., Bolker, B., and Walker, S. (2015). Fitting Linear Mixed-Effects
1171 Models Using lme4. Journal of Statistical Software; Vol 1, Issue 1 (2015).
1172 Bertzbach, L.D., Vladimirova, D., Dietert, K., Abdelgawad, A., Gruber, A.D.,
1173 Osterrieder, N., and Trimpert, J. (2020). SARS-CoV-2 infection of Chinese hamsters
1174 (Cricetulus griseus) reproduces COVID-19 pneumonia in a well-established small
1175 animal model. Transbound Emerg Dis.
1176 Blaszczyk, J., Coillie, E.V., Proost, P., Damme, J.V., Opdenakker, G., Bujacz, G.D.,
1177 Wang, J.M., and Ji, X. (2000). Complete crystal structure of monocyte chemotactic
1178 protein-2, a CC chemokine that interacts with multiple receptors. Biochemistry *39*,
1179 14075-14081.
1180 Briseno, C.G., Haldar, M., Kretzer, N.M., Wu, X., Theisen, D.J., Kc, W., Durai, V.,
1181 Grajales-Reyes, G.E., Iwata, A., Bagadia, P.*, et al.* (2016). Distinct Transcriptional
1182 Programs Control Cross-Priming in Classical and Monocyte-Derived Dendritic Cells.
1183 Cell Rep *15*, 2462-2474.
1184 Burgess, M., Wicks, K., Gardasevic, M., and Mace, K.A. (2019). Cx3CR1 Expression
1185 Identifies Distinct Macrophage Populations That Contribute Differentially to
1186 Inflammation and Repair. Immunohorizons *3*, 262-273.
1187 Butler, A., Hoffman, P., Smibert, P., Papalexi, E., and Satija, R. (2018). Integrating
1188 single-cell transcriptomic data across different conditions, technologies, and species.
1189 Nat Biotechnol *36*, 411-420.
1190 Cantuti-Castelvetri, L., Ojha, R., Pedro, L.D., Djannatian, M., Franz, J., Kuivanen, S.,
1191 van der Meer, F., Kallio, K., Kaya, T., Anastasina, M.*, et al.* (2020). Neuropilin-1
1192 facilitates SARS-CoV-2 cell entry and infectivity. Science *370*, 856-860.

Cao, Z., Lis, R., Ginsberg, M., Chavez, D., Shido, K., Rabbany, S.Y., Fong, G.H., Sakmar, T.P., Rafii, S., and Ding, B.S. (2016). Targeting of the pulmonary capillary vascular niche promotes lung alveolar repair and ameliorates fibrosis. Nat Med *22*, 154-162.

Chiabrando, D., Mercurio, S., and Tolosano, E. (2014). Heme and erythropoieis: more than a structural role. Haematologica *99*, 973-983.

Chua, R.L., Lukassen, S., Trump, S., Hennig, B.P., Wendisch, D., Pott, F., Debnath, O., Thurmann, L., Kurth, F., Volker, M.T.*, et al.* (2020). COVID-19 severity correlates with airway epithelium-immune cell interactions identified by single-cell analysis. Nat Biotechnol *38*, 970-979.

Cochain, C., Vafadarnejad, E., Arampatzi, P., Pelisek, J., Winkels, H., Ley, K., Wolf, D., Saliba, A.E., and Zernecke, A. (2018). Single-Cell RNA-Seq Reveals the Transcriptional Landscape and Heterogeneity of Aortic Macrophages in Murine Atherosclerosis. Circ Res *122*, 1661-1674.

Cohen, M., Giladi, A., Gorki, A.D., Solodkin, D.G., Zada, M., Hladik, A., Miklosi, A., Salame, T.M., Halpern, K.B., David, E.*, et al.* (2018). Lung Single-Cell Signaling Interaction Map Reveals Basophil Role in Macrophage Imprinting. Cell *175*, 1031-1044 e1018.

Cox, J., Hein, M.Y., Luber, C.A., Paron, I., Nagaraj, N., and Mann, M. (2014). Accurate proteome-wide label-free quantification by delayed normalization and maximal peptide ratio extraction, termed MaxLFQ. Mol Cell Proteomics *13*, 2513-2526.

Daly, J.L., Simonetti, B., Klein, K., Chen, K.E., Williamson, M.K., Anton-Plagaro, C., Shoemark, D.K., Simon-Gracia, L., Bauer, M., Hollandi, R.*, et al.* (2020). Neuropilin-1 is a host factor for SARS-CoV-2 infection. Science *370*, 861-865.

Davies, J., Randeva, H.S., Chatha, K., Hall, M., Spandidos, D.A., Karteris, E., and Kyrou, I. (2020). Neuropilin1 as a new potential SARSCoV2 infection mediator implicated in the neurologic features and central nervous system involvement of COVID19. Mol Med Rep *22*, 4221-4226.

Demichev, V., Messner, C.B., Vernardis, S.I., Lilley, K.S., and Ralser, M. (2020a). DIA-NN: neural networks and interference correction enable deep proteome coverage in high throughput. Nat Methods *17*, 41-44.

Demichev, V., Tober-Lau, P., Nazarenko, T., Thibeault, C., Whitwell, H., Lemke, O., Röhl, A., Freiwald, A., Szyrwiel, L., Ludwig, D.*, et al.* (2020b). A time-resolved

proteomic and diagnostic map characterizes COVID-19 disease progression and predicts outcome. medRxiv, 2020.2011.2009.20228015.

Dietert, K., Gutbier, B., Wienhold, S.M., Reppe, K., Jiang, X., Yao, L., Chaput, C., Naujoks, J., Brack, M., Kupke, A.*, et al.* (2017). Spectrum of pathogen- and model-specific histopathologies in mouse models of acute pneumonia. PLoS One *12*, e0188251.

Durinck, S., Spellman, P.T., Birney, E., and Huber, W. (2009). Mapping identifiers for the integration of genomic datasets with the R/Bioconductor package biomaRt. Nat Protoc *4*, 1184-1191.

Durussel, J., Haile, D.W., Mooses, K., Daskalaki, E., Beattie, W., Mooses, M., Mekonen, W., Ongaro, N., Anjila, E., Patel, R.K.*, et al.* (2016). Blood transcriptional signature of recombinant human erythropoietin administration and implications for antidoping strategies. Physiol Genomics *48*, 202-209.

Dutertre, C.A., Becht, E., Irac, S.E., Khalilnezhad, A., Narang, V., Khalilnezhad, S., Ng, P.Y., van den Hoogen, L.L., Leong, J.Y., Lee, B.*, et al.* (2019). Single-Cell Analysis of Human Mononuclear Phagocytes Reveals Subset-Defining Markers and Identifies Circulating Inflammatory Dendritic Cells. Immunity *51*, 573-589 e578.

El-Gedaily, A., Schoedon, G., Schneemann, M., and Schaffner, A. (2004). Constitutive and regulated expression of platelet basic protein in human monocytes. J Leukoc Biol *75*, 495-503.

Escher, R., Breakey, N., and Lammle, B. (2020). Severe COVID-19 infection associated with endothelial activation. Thromb Res *190*, 62.

Fiege, J.K., Thiede, J.M., Nanda, H., Matchett, W.E., Moore, P.J., Montanari, N.R., Thielen, B.K., Daniel, J., Stanley, E., Hunter, R.C.*, et al.* (2020). Single cell resolution of SARS-CoV-2 tropism, antiviral responses, and susceptibility to therapies in primary human airway epithelium. bioRxiv, 2020.2010.2019.343954.

Ford, J., Hughson, A., Lim, K., Bardina, S.V., Lu, W., Charo, I.F., Lim, J.K., and Fowell, D.J. (2018). CCL7 Is a Negative Regulator of Cutaneous Inflammation Following Leishmania major Infection. Front Immunol *9*, 3063.

Franzen, O., Gan, L.M., and Bjorkegren, J.L.M. (2019). PanglaoDB: a web server for exploration of mouse and human single-cell RNA sequencing data. Database (Oxford) *2019*.

Fu, J., Kong, J., Wang, W., Wu, M., Yao, L., Wang, Z., Jin, J., Wu, D., and Yu, X. (2020). The clinical implication of dynamic neutrophil to lymphocyte ratio and D-dimer in COVID-19: A retrospective study in Suzhou China. Thromb Res *192*, 3-8.

Gaidatzis, D., Lerch, A., Hahne, F., and Stadler, M.B. (2015). QuasR: quantification and annotation of short reads in R. Bioinformatics *31*, 1130-1132.

Gong, S.R., and Bao, L.L. (2018). The battle against SARS and MERS coronaviruses: Reservoirs and Animal Models. Animal Model Exp Med *1*, 125-133.

Gretebeck, L.M., and Subbarao, K. (2015). Animal models for SARS and MERS coronaviruses. Curr Opin Virol *13*, 123-129.

Gruber, A.D., Osterrieder, N., Bertzbach, L.D., Vladimirova, D., Greuel, S., Ihlow, J., Horst, D., Trimpert, J., and Dietert, K. (2020). Standardization of Reporting Criteria for Lung Pathology in SARS-CoV-2-infected Hamsters: What Matters? Am J Respir Cell Mol Biol *63*, 856-859.

Guan, W.J., Ni, Z.Y., Hu, Y., Liang, W.H., Ou, C.Q., He, J.X., Liu, L., Shan, H., Lei, C.L., Hui, D.S.C.*, et al.* (2020). Clinical Characteristics of Coronavirus Disease 2019 in China. N Engl J Med *382*, 1708-1720.

Gudbjartsson, D.F., Norddahl, G.L., Melsted, P., Gunnarsdottir, K., Holm, H., Eythorsson, E., Arnthorsson, A.O., Helgason, D., Bjarnadottir, K., Ingvarsson, R.F.*, et al.* (2020). Humoral Immune Response to SARS-CoV-2 in Iceland. N Engl J Med *383*, 1724-1734.

Han, X., Wang, R., Zhou, Y., Fei, L., Sun, H., Lai, S., Saadatpour, A., Zhou, Z., Chen, H., Ye, F.*, et al.* (2018). Mapping the Mouse Cell Atlas by Microwell-Seq. Cell *172*, 1091-1107 e1017.

Hönzke, K., Obermayer, B., Mache, C., Fatykhova, D., Kessler, M., Dökel, S., Wyler, E., Hoffmann, K., Schulze, J., Mieth, M.*, et al.* (2020). Human Lungs Show Limited Permissiveness for SARS-CoV-2 Due to Scarce ACE2 Levels But Strong Virus-Induced Immune Activation in Alveolar Macrophages. SSRN.

Hou, Y.J., Okuda, K., Edwards, C.E., Martinez, D.R., Asakura, T., Dinnon, K.H., 3rd, Kato, T., Lee, R.E., Yount, B.L., Mascenik, T.M.*, et al.* (2020). SARS-CoV-2 Reverse Genetics Reveals a Variable Infection Gradient in the Respiratory Tract. Cell *182*, 429-446 e414.

Imai, M., Iwatsuki-Horimoto, K., Hatta, M., Loeber, S., Halfmann, P.J., Nakajima, N., Watanabe, T., Ujie, M., Takahashi, K., Ito, M.*, et al.* (2020). Syrian hamsters as a

small animal model for SARS-CoV-2 infection and countermeasure development. Proc Natl Acad Sci U S A *117*, 16587-16595.

Janice Oh, H.L., Ken-En Gan, S., Bertoletti, A., and Tan, Y.J. (2012). Understanding the T cell immune response in SARS coronavirus infection. Emerg Microbes Infect *1*, e23.

Jiang, R.D., Liu, M.Q., Chen, Y., Shan, C., Zhou, Y.W., Shen, X.R., Li, Q., Zhang, L., Zhu, Y., Si, H.R.*, et al.* (2020). Pathogenesis of SARS-CoV-2 in Transgenic Mice Expressing Human Angiotensin-Converting Enzyme 2. Cell *182*, 50-58 e58.

Johansen, M.D., Irving, A., Montagutelli, X., Tate, M.D., Rudloff, I., Nold, M.F., Hansbro, N.G., Kim, R.Y., Donovan, C., Liu, G.*, et al.* (2020). Animal and translational models of SARS-CoV-2 infection and COVID-19. Mucosal Immunol *13*, 877-891.

Khoury, D.S., Wheatley, A.K., Ramuta, M.D., Reynaldi, A., Cromer, D., Subbarao, K., O'Connor, D.H., Kent, S.J., and Davenport, M.P. (2020). Measuring immunity to SARS-CoV-2 infection: comparing assays and animal models. Nat Rev Immunol *20*, 727-738.

Kim, D., Paggi, J.M., Park, C., Bennett, C., and Salzberg, S.L. (2019). Graph-based genome alignment and genotyping with HISAT2 and HISAT-genotype. Nat Biotechnol *37*, 907-915.

Kim, M.H., Yang, D., Kim, M., Kim, S.Y., Kim, D., and Kang, S.J. (2017). A late-lineage murine neutrophil precursor population exhibits dynamic changes during demand-adapted granulopoiesis. Sci Rep *7*, 39804.

Kolberg, L., and Raudvere, U. (2020). gprofiler2: Interface to the 'g:Profiler' Toolset.

Kreye, J., Reincke, S.M., Kornau, H.C., Sanchez-Sendin, E., Corman, V.M., Liu, H., Yuan, M., Wu, N.C., Zhu, X., Lee, C.D.*, et al.* (2020a). A Therapeutic Non-self-reactive SARS-CoV-2 Antibody Protects from Lung Pathology in a COVID-19 Hamster Model. Cell *183*, 1058-1069 e1019.

Kreye, J., Reincke, S.M., Kornau, H.C., Sanchez-Sendin, E., Max Corman, V., Liu, H., Yuan, M., Wu, N.C., Zhu, X., Lee, C.D.*, et al.* (2020b). A SARS-CoV-2 neutralizing antibody protects from lung pathology in a COVID-19 hamster model. bioRxiv.

Lagunas-Rangel, F.A. (2020). Neutrophil-to-lymphocyte ratio and lymphocyte-to-C-reactive protein ratio in patients with severe coronavirus disease 2019 (COVID-19): A meta-analysis. J Med Virol *92*, 1733-1734.

Lechner, A.J., Driver, I.H., Lee, J., Conroy, C.M., Nagle, A., Locksley, R.M., and Rock, J.R. (2017). Recruited Monocytes and Type 2 Immunity Promote Lung Regeneration following Pneumonectomy. Cell Stem Cell *21*, 120-134 e127.

Lee, A.C., Zhang, A.J., Chan, J.F., Li, C., Fan, Z., Liu, F., Chen, Y., Liang, R., Sridhar, S., Cai, J.P.*, et al.* (2020). Oral SARS-CoV-2 Inoculation Establishes Subclinical Respiratory Infection with Virus Shedding in Golden Syrian Hamsters. Cell Rep Med *1*, 100121.

Lee, H.S., Choi, J., Son, T., Wee, H.J., Bae, S.J., Seo, J.H., Park, J.H., Ryu, S.H., Lee, D., Jang, M.K.*, et al.* (2018). Altered AKAP12 expression in portal fibroblasts and liver sinusoids mediates transition from hepatic fibrogenesis to fibrosis resolution. Exp Mol Med *50*, 48.

Liao, M., Liu, Y., Yuan, J., Wen, Y., Xu, G., Zhao, J., Cheng, L., Li, J., Wang, X., Wang, F.*, et al.* (2020). Single-cell landscape of bronchoalveolar immune cells in patients with COVID-19. Nat Med *26*, 842-844.

Liberzon, A., Birger, C., Thorvaldsdottir, H., Ghandi, M., Mesirov, J.P., and Tamayo, P. (2015). The Molecular Signatures Database (MSigDB) hallmark gene set collection. Cell Syst *1*, 417-425.

Liu, J., Li, S., Liang, B., Wang, X., Wang, H., Li, W., Tong, Q., Yi, J., Zhao, L., Xiong, L.*, et al.* (2020). Longitudinal characteristics of lymphocyte responses and cytokine profiles in the peripheral blood of SARS-CoV-2 infected patients. EBioMedicine *55*, 102763.

Liu, T., Zhang, L., Joo, D., and Sun, S.C. (2017). NF-kappaB signaling in inflammation. Signal Transduct Target Ther *2*.

Mammoto, A., and Mammoto, T. (2019). Vascular Niche in Lung Alveolar Development, Homeostasis, and Regeneration. Front Bioeng Biotechnol *7*, 318.

Marchetti, M. (2020). COVID-19-driven endothelial damage: complement, HIF-1, and ABL2 are potential pathways of damage and targets for cure. Ann Hematol *99*, 1701-1707.

Merad, M., and Martin, J.C. (2020). Pathological inflammation in patients with COVID-19: a key role for monocytes and macrophages. Nat Rev Immunol *20*, 355-362.

Messner, C.B., Demichev, V., Bloomfield, N., White, M., Kreidl, M., Ivosev, G., Wasim, F., Zelezniak, A., Lilley, K.S., Tate, S.*, et al.* (2020a). Scanning SWATH

1359 acquisition enables high-throughput proteomics with chromatographic gradients as
1360 fast as 30 seconds. bioRxiv, 656793.
1361 Messner, C.B., Demichev, V., Wendisch, D., Michalick, L., White, M., Freiwald, A.,
1362 Textoris-Taube, K., Vernardis, S.I., Egger, A.S., Kreidl, M.*, et al.* (2020b). Ultra-High-
1363 Throughput Clinical Proteomics Reveals Classifiers of COVID-19 Infection. Cell Syst
1364 *11*, 11-24 e14.
1365 Michalick, L., Weidenfeld, S., Grimmer, B., Fatykhova, D., Solymosi, P.D., Behrens,
1366 F., Dohmen, M., Brack, M.C., Schulz, S., Thomasch, E.*, et al.* (2020). Plasma
1367 mediators in patients with severe COVID-19 cause lung endothelial barrier failure.
1368 Eur Respir J.
1369 Middleton, E.A., He, X.Y., Denorme, F., Campbell, R.A., Ng, D., Salvatore, S.P.,
1370 Mostyka, M., Baxter-Stoltzfus, A., Borczuk, A.C., Loda, M.*, et al.* (2020). Neutrophil
1371 extracellular traps contribute to immunothrombosis in COVID-19 acute respiratory
1372 distress syndrome. Blood *136*, 1169-1179.
1373 Monaghan, K.L., Zheng, W., Hu, G., and Wan, E.C.K. (2019). Monocytes and
1374 Monocyte-Derived Antigen-Presenting Cells Have Distinct Gene Signatures in
1375 Experimental Model of Multiple Sclerosis. Front Immunol *10*, 2779.
1376 Morse, C., Tabib, T., Sembrat, J., Buschur, K.L., Bittar, H.T., Valenzi, E., Jiang, Y.,
1377 Kass, D.J., Gibson, K., Chen, W.*, et al.* (2019). Proliferating SPP1/MERTK-
1378 expressing macrophages in idiopathic pulmonary fibrosis. Eur Respir J *54*.
1379 Muller, T., Kalxdorf, M., Longuespee, R., Kazdal, D.N., Stenzinger, A., and
1380 Krijgsveld, J. (2020). Automated sample preparation with SP3 for low-input clinical
1381 proteomics. Mol Syst Biol *16*, e9111.
1382 Ni, L., Ye, F., Cheng, M.L., Feng, Y., Deng, Y.Q., Zhao, H., Wei, P., Ge, J., Gou, M.,
1383 Li, X.*, et al.* (2020). Detection of SARS-CoV-2-Specific Humoral and Cellular
1384 Immunity in COVID-19 Convalescent Individuals. Immunity *52*, 971-977 e973.
1385 Niethamer, T.K., Stabler, C.T., Leach, J.P., Zepp, J.A., Morley, M.P., Babu, A., Zhou,
1386 S., and Morrisey, E.E. (2020). Defining the role of pulmonary endothelial cell
1387 heterogeneity in the response to acute lung injury. Elife *9*.
1388 Olajuyin, A.M., Zhang, X., and Ji, H.L. (2019). Alveolar type 2 progenitor cells for lung
1389 injury repair. Cell Death Discov *5*, 63.
1390 Osterrieder, N., Bertzbach, L.D., Dietert, K., Abdelgawad, A., Vladimirova, D., Kunec,
1391 D., Hoffmann, D., Beer, M., Gruber, A.D., and Trimpert, J. (2020). Age-Dependent
1392 Progression of SARS-CoV-2 Infection in Syrian Hamsters. Viruses *12*.

1393 Palumbo-Zerr, K., Zerr, P., Distler, A., Fliehr, J., Mancuso, R., Huang, J., Mielenz, D.,
1394 Tomcik, M., Furnrohr, B.G., Scholtysek, C.*, et al.* (2015). Orphan nuclear receptor
1395 NR4A1 regulates transforming growth factor-beta signaling and fibrosis. Nat Med *21*,
1396 150-158.
1397 Peng, Y., Mentzer, A.J., Liu, G., Yao, X., Yin, Z., Dong, D., Dejnirattisai, W., Rostron,
1398 T., Supasa, P., Liu, C.*, et al.* (2020). Broad and strong memory CD4(+) and CD8(+) T
1399 cells induced by SARS-CoV-2 in UK convalescent individuals following COVID-19.
1400 Nat Immunol *21*, 1336-1345.
1401 Praktiknjo, S.D., Obermayer, B., Zhu, Q., Fang, L., Liu, H., Quinn, H., Stoeckius, M.,
1402 Kocks, C., Birchmeier, W., and Rajewsky, N. (2020). Tracing tumorigenesis in a solid
1403 tumor model at single-cell resolution. Nat Commun *11*, 991.
1404 R Core Team (2019). R: A language and environment for statistical computing
1405 (Vienna, Austria: R Foundation for Statistical Computing).
1406 Raredon, M.S.B., Adams, T.S., Suhail, Y., Schupp, J.C., Poli, S., Neumark, N., Leiby,
1407 K.L., Greaney, A.M., Yuan, Y., Horien, C.*, et al.* (2019). Single-cell connectomic
1408 analysis of adult mammalian lungs. Sci Adv *5*, eaaw3851.
1409 Ritchie, M.E., Phipson, B., Wu, D., Hu, Y., Law, C.W., Shi, W., and Smyth, G.K.
1410 (2015). limma powers differential expression analyses for RNA-sequencing and
1411 microarray studies. Nucleic Acids Res *43*, e47.
1412 Roberts, A., Vogel, L., Guarner, J., Hayes, N., Murphy, B., Zaki, S., and Subbarao, K.
1413 (2005). Severe acute respiratory syndrome coronavirus infection of golden Syrian
1414 hamsters. J Virol *79*, 503-511.
1415 Rodrigues, P.F., Alberti-Servera, L., Eremin, A., Grajales-Reyes, G.E., Ivanek, R.,
1416 and Tussiwand, R. (2018). Distinct progenitor lineages contribute to the
1417 heterogeneity of plasmacytoid dendritic cells. Nat Immunol *19*, 711-722.
1418 Ronning, K.E., Karlen, S.J., Miller, E.B., and Burns, M.E. (2019). Molecular profiling
1419 of resident and infiltrating mononuclear phagocytes during rapid adult retinal
1420 degeneration using single-cell RNA sequencing. Sci Rep *9*, 4858.
1421 Sampath, P., Moideen, K., Ranganathan, U.D., and Bethunaickan, R. (2018).
1422 Monocyte Subsets: Phenotypes and Function in Tuberculosis Infection. Front
1423 Immunol *9*, 1726.
1424 Schauer, A.E., Klassert, T.E., von Lachner, C., Riebold, D., Schneeweiss, A., Stock,
1425 M., Muller, M.M., Hammerschmidt, S., Bufler, P., Seifert, U.*, et al.* (2017). IL-37

Causes Excessive Inflammation and Tissue Damage in Murine Pneumococcal Pneumonia. J Innate Immun *9*, 403-418.

Schneider, W.M., Chevillotte, M.D., and Rice, C.M. (2014). Interferon-stimulated genes: a complex web of host defenses. Annu Rev Immunol *32*, 513-545.

Schnoor, M., Alcaide, P., Voisin, M.B., and van Buul, J.D. (2015). Crossing the Vascular Wall: Common and Unique Mechanisms Exploited by Different Leukocyte Subsets during Extravasation. Mediators Inflamm *2015*, 946509.

Schoggins, J.W. (2019). Interferon-Stimulated Genes: What Do They All Do? Annu Rev Virol *6*, 567-584.

Schulte-Schrepping, J., Reusch, N., Paclik, D., Bassler, K., Schlickeiser, S., Zhang, B., Kramer, B., Krammer, T., Brumhard, S., Bonaguro, L.*, et al.* (2020). Severe COVID-19 Is Marked by a Dysregulated Myeloid Cell Compartment. Cell *182*, 1419-1440 e1423.

Shaheen, Z.R., Christmann, B.S., Stafford, J.D., Moran, J.M., Buller, R.M.L., and Corbett, J.A. (2019). CCR5 is a required signaling receptor for macrophage expression of inflammatory genes in response to viral double-stranded RNA. Am J Physiol Regul Integr Comp Physiol *316*, R525-R534.

Shin, H.S., Kim, Y., Kim, G., Lee, J.Y., Jeong, I., Joh, J.S., Kim, H., Chang, E., Sim, S.Y., Park, J.S.*, et al.* (2019). Immune Responses to Middle East Respiratory Syndrome Coronavirus During the Acute and Convalescent Phases of Human Infection. Clin Infect Dis *68*, 984-992.

Sia, S.F., Yan, L.M., Chin, A.W.H., Fung, K., Choy, K.T., Wong, A.Y.L., Kaewpreedee, P., Perera, R., Poon, L.L.M., Nicholls, J.M.*, et al.* (2020). Pathogenesis and transmission of SARS-CoV-2 in golden hamsters. Nature *583*, 834-838.

Smith, S.L., Kennedy, P.R., Stacey, K.B., Worboys, J.D., Yarwood, A., Seo, S., Solloa, E.H., Mistretta, B., Chatterjee, S.S., Gunaratne, P.*, et al.* (2020). Diversity of peripheral blood human NK cells identified by single-cell RNA sequencing. Blood Adv *4*, 1388-1406.

Speranza, E., Williamson, B., Feldmann, F., Sturdevant, G., Perez-Perez, L., Meade-White, K., Smith, B.J., Lovaglio, J., Martens, C., Munster, V.*, et al.* (2020). SARS-CoV-2 Infection Dynamics in Lungs of African Green Monkeys. SSRN.

1458 Stuart, T., Butler, A., Hoffman, P., Hafemeister, C., Papalexi, E., Mauck, W.M., 3rd,
1459 Hao, Y., Stoeckius, M., Smibert, P., and Satija, R. (2019). Comprehensive Integration
1460 of Single-Cell Data. Cell *177*, 1888-1902 e1821.
1461 Subbarao, K., and Roberts, A. (2006). Is there an ideal animal model for SARS?
1462 Trends Microbiol *14*, 299-303.
1463 Tabula Muris Consortium (2018). Single-cell transcriptomics of 20 mouse organs
1464 creates a Tabula Muris. Nature *562*, 367-372.
1465 Tawfik, O., Rao, D., Nothnick, W.B., Graham, A., Mau, B., and Fan, F. (2014).
1466 Transgelin, a Novel Marker of Smooth Muscle Differentiation, Effectively
1467 Distinguishes Endometrial Stromal Tumors from Uterine Smooth Muscle Tumors. Int
1468 J Gynecol Obstet Reprod Med Res *1*, 26-31.
1469 Thompson, B.T., Chambers, R.C., and Liu, K.D. (2017). Acute Respiratory Distress
1470 Syndrome. N Engl J Med *377*, 562-572.
1471 To, K.F., and Lo, A.W. (2004). Exploring the pathogenesis of severe acute
1472 respiratory syndrome (SARS): the tissue distribution of the coronavirus (SARS-CoV)
1473 and its putative receptor, angiotensin-converting enzyme 2 (ACE2). J Pathol *203*,
1474 740-743.
1475 Tostanoski, L.H., Wegmann, F., Martinot, A.J., Loos, C., McMahan, K., Mercado,
1476 N.B., Yu, J., Chan, C.N., Bondoc, S., Starke, C.E.*, et al.* (2020). Ad26 vaccine
1477 protects against SARS-CoV-2 severe clinical disease in hamsters. Nat Med *26*,
1478 1694-1700.
1479 Travaglini, K.J., Nabhan, A.N., Penland, L., Sinha, R., Gillich, A., Sit, R.V., Chang, S.,
1480 Conley, S.D., Mori, Y., Seita, J.*, et al.* (2020). A molecular cell atlas of the human
1481 lung from single-cell RNA sequencing. Nature *587*, 619-625.
1482 Trimpert, J., Vladimirova, D., Dietert, K., Abdelgawad, A., Kunec, D., Dokel, S., Voss,
1483 A., Gruber, A.D., Bertzbach, L.D., and Osterrieder, N. (2020). The Roborovski Dwarf
1484 Hamster Is A Highly Susceptible Model for a Rapid and Fatal Course of SARS-CoV-2
1485 Infection. Cell Rep *33*, 108488.
1486 V'Kovski, P., Kratzel, A., Steiner, S., Stalder, H., and Thiel, V. (2020). Coronavirus
1487 biology and replication: implications for SARS-CoV-2. Nat Rev Microbiol.
1488 Van Strijp, J.A., Van Kessel, K.P., van der Tol, M.E., and Verhoef, J. (1989).
1489 Complement-mediated phagocytosis of herpes simplex virus by granulocytes.
1490 Binding or ingestion. J Clin Invest *84*, 107-112.

1491 Varchetta, S., Mele, D., Oliviero, B., Mantovani, S., Ludovisi, S., Cerino, A., Bruno,
1492 R., Castelli, A., Mosconi, M., Vecchia, M.*, et al.* (2020). Unique immunological profile
1493 in patients with COVID-19. Cell Mol Immunol.
1494 Wickham, H., Averick, M., Bryan, J., Chang, W., McGowan, L.D.A., François, R.,
1495 Grolemund, G., Hayes, A., Henry, L., Hester, J.*, et al.* (2019). Welcome to the
1496 Tidyverse. Journal of Open Source Software *4*, 1686.
1497 Winkler, E.S., Bailey, A.L., Kafai, N.M., Nair, S., McCune, B.T., Yu, J., Fox, J.M.,
1498 Chen, R.E., Earnest, J.T., Keeler, S.P.*, et al.* (2020). SARS-CoV-2 infection of
1499 human ACE2-transgenic mice causes severe lung inflammation and impaired
1500 function. Nat Immunol *21*, 1327-1335.
1501 Wyler, E., Mösbauer, K., Franke, V., Diag, A., Gottula Lina, T., Arsie, R., Klironomos,
1502 F., Koppstein, D., Ayoub, S., Buccitelli, C.*, et al.* (2020). Bulk and single-cell gene
1503 expression profiling of SARS-CoV-2 infected human cell lines identifies molecular
1504 targets for therapeutic intervention. bioRxiv, 2020.2005.2005.079194.
1505 Xie, X., Shi, Q., Wu, P., Zhang, X., Kambara, H., Su, J., Yu, H., Park, S.Y., Guo, R.,
1506 Ren, Q.*, et al.* (2020). Single-cell transcriptome profiling reveals neutrophil
1507 heterogeneity in homeostasis and infection. Nat Immunol *21*, 1119-1133.
1508 Zeng, H.L., Chen, D., Yan, J., Yang, Q., Han, Q.Q., Li, S.S., and Cheng, L. (2020).
1509 Proteomic characteristics of bronchoalveolar lavage fluid in critical COVID-19
1510 patients. FEBS J.
1511 Zhang, X., Lan, Y., Xu, J., Quan, F., Zhao, E., Deng, C., Luo, T., Xu, L., Liao, G.,
1512 Yan, M.*, et al.* (2019). CellMarker: a manually curated resource of cell markers in
1513 human and mouse. Nucleic Acids Res *47*, D721-D728.
1514 Zhao, Y., Li, X., Zhao, W., Wang, J., Yu, J., Wan, Z., Gao, K., Yi, G., Wang, X., Fan,
1515 B.*, et al.* (2019). Single-cell transcriptomic landscape of nucleated cells in umbilical
1516 cord blood. Gigascience *8*.
1517 Zhu, P., Martinvalet, D., Chowdhury, D., Zhang, D., Schlesinger, A., and Lieberman,
1518 J. (2009). The cytotoxic T lymphocyte protease granzyme A cleaves and inactivates
1519 poly(adenosine 5'-diphosphate-ribose) polymerase-1. Blood *114*, 1205-1216.
1520 Zuccolo, J., Deng, L., Unruh, T.L., Sanyal, R., Bau, J.A., Storek, J., Demetrick, D.J.,
1521 Luider, J.M., Auer-Grzesiak, I.A., Mansoor, A.*, et al.* (2013). Expression of MS4A and
1522 TMEM176 Genes in Human B Lymphocytes. Front Immunol *4*, 195.

1523 Zyla, J., Marczyk, M., Domaszewska, T., Kaufmann, S.H.E., Polanska, J., and
1524 Weiner, J. (2019). Gene set enrichment for reproducible science: comparison of
1525 CERNO and eight other algorithms. Bioinformatics *35*, 5146-5154.
1526